PHYSICAL REVIEW E **75**, 011108 (2007)

Extension of scaled particle theory to inhomogeneous hard particle fluids. III. Entropic force exerted on a cavity that intersects a hard wall

Daniel W. Siderius and David S. Corti*
School of Chemical Engineering, Purdue University, 480 Stadium Mall Drive, West Lafayette, Indiana 47907-2100, USA

(Received 21 September 2006; published 11 January 2007)

We present a further development of an inhomogeneous scaled particle theory (I-SPT) for hard particle fluids confined by hard walls, such that the reversible work of cavity insertion can now be determined for all cavities that intersect one of the walls. Building upon a previous version of I-SPT [D. W. Siderius and D. S. Corti, Phys. Rev. E, **71**, 036141 (2005)], a new function, $\bar{F}$, is introduced, which is proportional to the net force on the surface of the cavity in the direction normal to the wall. The reversible work of cavity insertion is then determined by an integral over the force required to "push" the cavity of fixed size into the fluid starting from a position behind the wall. An exact relation for $\bar{F}$ at certain cavity locations and radii is derived and an accurate interpolation scheme is proposed for the computation of $\bar{F}$ beyond these exact limits. The chosen interpolation incorporates a large number of exact and nearly exact conditions, several of which follow from the surface thermodynamics of macroscopic cavities. Work predictions using $\bar{F}$ are highly accurate as compared to simulation results at low to moderate fluid densities. Good agreement still persists at densities near the hard-sphere freezing transition. The interpolation of $\bar{F}$ is also used to estimate the depletion force between a hard sphere solute and the wall. The I-SPT entropic force predictions are in good agreement with simulation results presented in the literature. Due to its reliance upon physical and geometric arguments, I-SPT provides important insights into the origin of various depletion effects such as how the interplay between geometry and the varying local density at the cavity surface gives rise to the appearance of multiple attractive regions at intermediate solute sizes and a universal repulsive region, both within solute to wall separations that are less than the diameter of a solvent particle. Finally, all of the scaled particle theory-based methods presented here can, in principle, be extended to describe hard particle fluids confined by nonplanar surfaces, thereby providing estimates of the depletion force between a solute and a variety of surfaces of interest.

DOI: 10.1103/PhysRevE.75.011108 PACS number(s): 05.70.Ce, 05.20.−y, 82.70.Dd, 05.70.Np

I. INTRODUCTION

Recently, the present authors developed an initial extension of scaled particle theory (SPT) to inhomogeneous hard particle fluids [1,2], where the nonuniform fluid density that develops near a hard, structureless wall is explicitly taken into account. New physical as well as geometric insights were generated into the structural changes brought about by the insertion of cavities near a wall. While successful, this version of inhomogeneous SPT, or I-SPT, was limited to those cases for which the cavity exposed to the nonuniform fluid near the wall has a volume equal to or less than that of a hemisphere. To extend the range of I-SPT, at least with respect to the types of systems that it can describe, one desires to consider cavities located at any distance from the wall, i.e., cavities beyond the hemisphere. Although work toward this goal is still in progress, we present here a further development of I-SPT in which the force on a cavity that still intersects the wall (actually the exclusion plane it generates for the hard-sphere fluid) is determined. Rather than growing a cavity radially at a given location, we instead consider the forces needed to "push" a cavity into the fluid when starting from a position behind the wall. This new route is chosen since it allows for the use of additional conditions within I-SPT and avoids some difficulties that arise if one were to focus on the growth of cavities. While our extension of I-SPT is similar to both bulk SPT [3] and the previous version of I-SPT, some key differences arise, leading to new conclusions and interpretations of I-SPT quantities.

Due to the equivalence of cavities and hard-sphere solutes, our I-SPT relations may also be used to predict the depletion, or entropic, force between a hard-sphere solute and a hard wall (for a particularly important range of solute-wall separations). Depletion forces are effective forces that arise in mixtures of colloids due to asymmetries in the local ordering of each colloidal species, much like a potential of mean force in a pure fluid [4–8]. Within various colloidal dispersions of interest, the interactions between colloids are often dominated by short-ranged repulsive forces, and as such are similar in nature to a dispersion of hard spheres. An SPT-based approach is therefore a natural starting point for the analysis of such systems. Since SPT has already yielded a large number of insights into the thermophysical properties of hard-sphere fluids, such as the importance of geometry in controlling hard-particle behavior [9–12], one suspects that both SPT and I-SPT should likewise provide useful information about the physical and geometric aspects of depletion interactions [4,5].

The development of accurate expressions for entropic forces are also of scientific and technical interest, given the importance of entropic interactions in governing the behavior of hard-sphere-like fluids [6,13–16] as well as the potential of depletion forces to control the self-assembly of colloidal systems [6,17]. SPT has previously been applied by Corti

---

*Electronic address: dscorti@ecn.purdue.edu and Reiss [18] to compute the depletion force between a hard colloid and a hard wall. Utilizing the surface thermodynamics of macroscopic cavities, these authors obtained relatively simple expressions for both the entropic potential and the entropic force. While reasonably accurate at low solvent packing fractions, their approach proved to be lacking at higher densities since it failed to account for the nonuniform density near the hard wall. Within the framework of surface thermodynamics, the free energy cost of changing the perimeter of the "three-phase" contact line (i.e., the intersection of the hard-sphere solvent, wall and the cavity), or line tension (a linear analogue of the surface tension), was not included in the analysis. (The neglecting of the line tension was not an oversight, however, since an expression for the line tension of the "three-phase" interface is currently not known. In contrast, the surface tension of a cavity within a hard-particle fluid can be determined using SPT quantities [19].) Developing an extension of SPT that is tailored specifically for hard-particle fluids confined between hard walls is one of the goals of the current paper. By explicitly including the effects of the nonuniform density into SPT, knowledge of the line tension is not required since it will already be accounted for in the resulting SPT relations.

Although I-SPT is well suited to studying depletion interactions, our focus does not, however, reside entirely with the estimation of entropic forces. Further development of I-SPT also serves to generate new insights into the behavior of confined fluids, just as traditional SPT was able to do for uniform fluids. And when an SPT-based expression for the line tension of hard-particle fluids is finally generated, I-SPT will provide the various relations needed to estimate this important quantity.

The paper is outlined as follows. SPT and I-SPT are briefly reviewed in Sec. II. In Sec. III, the extension of I-SPT is presented, where a function describing the net force on the cavity surface is introduced. Exact relations for this I-SPT function are derived and the interpolation scheme utilized to represent this function beyond the exact limits is discussed. The simulation methods used to generate data for comparison to I-SPT predictions are outlined in Sec. IV. The application of the I-SPT relations to predicting depletion forces is presented in Sec. VI. In Sec. VII, some interesting geometric features of the new version of I-SPT are discussed. Conclusions are contained within Sec. VIII. Two appendixes also introduce and verify several conditions that are used within our proposed interpolation scheme.

II. ESSENTIAL FEATURES OF SPT

Before deriving several additional inhomogeneous SPT expressions, we briefly review some of the relations of bulk (homogeneous) SPT [3] as well as provide an overview of the already existing version of I-SPT [1,2]. More complete and detailed reviews of both forms of SPT may be found in Refs. [1,20–22]. To begin, we note that a basic concept of any version of SPT is the equivalence of hard-sphere particles and cavities. Within the hard-sphere fluid, a cavity is defined as a spherical region devoid of solvent hard-sphere centers. Consequently, a hard sphere solute of diameter σ_s in a fluid of solvent hard spheres of diameter σ is equivalent to and concentric with a cavity of radius λ, where $\lambda=(\sigma_s+\sigma)/2$ [3]. A cavity becomes equivalent to another solvent hard sphere when $\lambda=\sigma$.

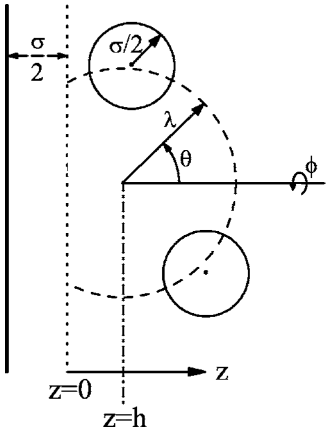

FIG. 1. Coordinate system used to describe cavities near a hard wall. The cavity (represented by the long-dashed line) of radius λ is centered at $z=h$. The z axis originates a distance $\sigma/2$ from the hard wall, where σ is the diameter of a hard-sphere solvent particle (represented by the solid circles; the centers of the hard-sphere solvent particles cannot access the region for which $z<0$). θ measures the angle originating from a line perpendicular to hard wall and colinear with the cavity center. ϕ describes the rotation around this line. Since the fluid is isotropic in the x and y directions, the system is symmetric about ϕ.

The central function of SPT for isotropic, unconfined hard-sphere fluids is $G(\lambda)$, where $\rho G(\lambda)$ is defined as the local density of hard-sphere centers at the surface of a cavity of radius λ and ρ is the density of hard-sphere centers far from the cavity [3]. Given that $\rho G(\lambda)kT$ is the local stress normal to the cavity surface (where T is the temperature and k is Boltzmann's constant), $G(\lambda)$ is related to $W(\lambda)$, the reversible work of adding a cavity of radius of at least λ, by [3]

$$W(\lambda) = 4\pi\rho kT\int_0^\lambda G(r)r^2dr. \tag{1}$$

For $\lambda \leqslant \sigma/2$, $G(\lambda)$ is known exactly. Beyond this limit, $G(\lambda)$ may be well represented by one or more interpolation functions between $\lambda=\sigma/2$ and $\lambda\to\infty$, each of which may utilize a number of exact conditions on $G(\lambda)$. If a single interpolation function is chosen, its usual form is that of a Laurent series in λ^{-1}, the number of terms and interpolation coefficients being determined by the number of conditions one imposes on $G(\lambda)$ [3,20,23]. Solving for these interpolation coefficients yields, among other quantities, an equation of state of the hard-sphere fluid, where we note that $G(\infty)=p/\rho kT$ (in which p is the pressure of the hard-sphere fluid).

When a hard-sphere fluid is confined by hard, planar walls, a cavity can now intersect either wall and, as illustrated in Fig. 1, may be less than full spheres when overlap occurs [1]. The inhomogeneities arising from the confining walls requires one to introduce a modified version of the SPT function $G(\lambda)$ since the local density of hard-sphere centers at the cavity surface is no longer spherically symmetric and also depends on the cavity's location (with respect to the walls). Here, the inhomogeneous SPT function $G(\lambda,\theta,h)$ is defined such that $\rho G(\lambda,\theta,h)$ is the local density of hard-sphere centers for the three identifying coordinates λ, θ, and h [1]. As shown in Fig. 1, λ is the cavity radius, θ identifies the angular position, and h locates the cavity relative to the hard wall (only cases in which $h \leqslant 0$ were considered in Ref. [1], ensuring that a cavity always overlapped the $z=0$ plane for any λ). For convenience, $G(\lambda,\theta,h)$ is averaged over θ to yield the function $\bar{G}(\lambda,h)$, which proves to be a more useful quantity. For example, $\bar{G}(\lambda,h)$ is known exactly in terms of the hard-sphere density profile, $\rho(z)$, for $\lambda \leqslant \sqrt{h^2+(\sigma/2)^2}$ (where z is the distance normal to the wall, see Fig. 1) and various conditions restrict its form for larger values of λ [1]. Similar to $G(\lambda)$, $\bar{G}(\lambda,h)$ is interpolated from $\lambda = \sqrt{h^2+(\sigma/2)^2}$ to $\lambda \to \infty$ by a Laurent series, but solving for the interpolation coefficients does not yield an equation of state in this case. In contrast, I-SPT requires an equation of state as input (which can be obtained, if desired, from bulk SPT [3]). A special case of I-SPT occurs when the cavity is a perfect hemisphere, or $h=0$. Another exact condition on $\bar{G}(\lambda,h)$ is then allowed [1], as compared to cavities in which $h<0$. For simplicity, the I-SPT function $\bar{G}(\lambda,h)$ is rewritten as $\bar{G}(\lambda)$ when $h=0$. Finally, analogous to bulk SPT, the reversible work of adding a cavity at the position $h \leqslant 0$ is given by [1]

$$W(\lambda,h) = 2\pi\rho kT\int_0^{\lambda} \bar{G}(r,h)(r^2 + rh)dr. \tag{2}$$

III. I-SPT: FORCE EXERTED ON A CAVITY THAT INTERSECTS A HARD WALL

The previous version of I-SPT only considered cavities located at $h \leqslant 0$. To enable I-SPT to describe cavities intersecting a hard wall for $h \geqslant 0$, a fundamentally different approach from the two earlier forms of SPT [1,3] is needed. Within each of these previous SPT versions, small cavities are first inserted at a particular location and then grown radially to the desired final size. Instead, our present method first begins with a cavity of desired size located at some distance behind the hard wall, which is then inserted into the fluid by "pushing" it at constant radius through the $z=0$ plane (Fig. 1). The reversible work needed to push the center of the cavity to a new location is related to an integral of the net force exerted on the cavity by the solvent. In what follows, we turn to the framework of I-SPT to derive a general expression for the net force on the surface of the cavity in terms of the I-SPT function $G(\lambda,\theta,h)$. We then determine an exact relation for this force under certain conditions and discuss the interpolation function needed, along with various conditions constraining its form, to describe the net force beyond the exact region.

Begin by considering a pure component hard-sphere fluid located near a hard, structureless wall. Our chosen coordinate system is again defined in Fig. 1, where the z axis originates a distance of $\sigma/2$ from the actual hard wall. Hence, the density of hard-sphere centers for $z<0$ is uniformly zero. For $z \geqslant 0$, the density profile is given by $\rho(z)$, beginning at $\rho(0) = p/kT$ and eventually oscillating and dampening to the interior bulk density ρ. For a given cavity of radius λ with a center located at $z=h$, we only consider configurations for which $-\lambda \leqslant h \leqslant \lambda$, ensuring that the cavity always intersects the $z=0$ plane. (No work is required to translate the cavity from a distance $h<-\lambda$ to $h=-\lambda$.)

Now, for any point on the surface of the cavity, the local stress normal to the cavity surface is again given by $\rho G(\lambda,\theta,h)kT$. The force exerted in the z direction on a differential area element is this local stress multiplied by both $\lambda^2 \sin\theta d\theta d\phi$ and $(-\cos\theta)$, the former being the differential area while the latter is the projection of the local stress in the negative z direction. Similar to other relations that have appeared before [9–11,24], the total force, $F(\lambda,h)$, on the cavity in the negative z direction follows from an integral over the cavity surface and is equal to

$$\begin{aligned} F(\lambda,h) &= -\int_0^{2\pi}\int_0^{\cos^{-1}(-h/\lambda)} \rho G(\lambda,\theta,h)kT\lambda^2 \sin\theta\cos\theta d\theta d\phi \\ &= -2\pi\rho kT\lambda^2\int_0^{\cos^{-1}(-h/\lambda)} G(\lambda,\theta,h)\sin\theta\cos\theta d\theta. \end{aligned} \tag{3}$$

In Eq. (3), the upper bound on θ is $\cos^{-1}(-h/\lambda)$, the θ angle at which the cavity intersects the $z=0$ plane. In terms of $F(\lambda,h)$, the reversible work of moving the center of a cavity of constant radius λ starting from $z=-\lambda$ to a final position h can now be written as

$$\begin{aligned} W(\lambda,h) &= -\int_{-\lambda}^{h} F(\lambda,z)dz \\ &= 2\pi\rho kT\lambda^2\int_{-\lambda}^{h} dz\int_0^{\cos^{-1}(-z/\lambda)} G(\lambda,\theta,z)\sin\theta\cos\theta d\theta. \end{aligned} \tag{4}$$

As noted above, the lower bound on the z integral in Eq. (4) is $z=-\lambda$ since a cavity centered at this position has not penetrated the fluid and, as such, the work of placing a cavity at that position is zero.

The expressions for F and W are not solvable without general knowledge of $G(\lambda,\theta,h)$. At present, the form of $G(\lambda,\theta,h)$ is known only for limited situations [2]. As a simplification, we introduce the function

$$\bar{F}(\lambda,h) = \int_0^{\cos^{-1}(-h/\lambda)} G(\lambda,\theta,h)\sin\theta\cos\theta d\theta, \tag{5}$$

which allows Eqs. (3) and (4) to be written very compactly as

$$F(\lambda,h) = -2\pi\rho kT\lambda^2\bar{F}(\lambda,h) \tag{6}$$

and

$$W(\lambda,h) = 2\pi\rho kT\lambda^2 \int_{-\lambda}^{h} \bar{F}(\lambda,z)dz. \tag{7}$$

A closer examination of Eq. (5) shows that $\bar{F}$ is proportional to the net force on the cavity surface due to collisions with the surrounding hard-sphere solvent particles. (Note that $\bar{F}$ is not an average pressure on the cavity surface, but simply a quantity proportional to the net force on the cavity surface.) $\bar{F}>0$ indicates that the net force is directed toward the wall, such that (positive) work must be performed to further push the cavity into the fluid or the cavity "feels" an attractive force in the negative z direction. $\bar{F}<0$ corresponds to a net force that is directed away from the wall, such that (negative) work is recovered upon further movement of the cavity or the cavity feels a repulsive force directed in the positive z direction. $\bar{F}$ can have different signs because collisions at a particular θ are weighted by $\sin\theta\cos\theta$. For $\theta<\pi/2$, the contribution of $G(\lambda,\theta,h)$ to $\bar{F}$ is always positive. For $\theta>\pi/2$, the contributions to $\bar{F}$ become negative. The sign of $\bar{F}$ therefore depends on which set of contributions is larger. Initially, $\bar{F}$ begins at a value of zero, $\bar{F}(\lambda,-\lambda)=0$, and then immediately becomes positive since θ never exceeds $\pi/2$ for $h<0$. When θ can exceed $\pi/2$ for $h>0$, some contributions to $\bar{F}(\lambda,h)$ become negative. We expect that these negative contributions will become larger in magnitude than the $\theta<\pi/2$ positive contributions, thereby yielding $\bar{F}(\lambda,h)<0$, since both attractive and repulsive depletion forces between a hard-sphere colloid and a flat surface have been reported, e.g., Ref. [24]. The local density enhancement that is known to develop around $\theta=\cos^{-1}(-h/\lambda)$ also reinforces this prediction, in which the density of hard-sphere centers for $\theta>\pi/2$ was shown to eventually outweigh the density of spheres contacting the surface for $\theta<\pi/2$ [2].

Similar to $G(\lambda)$ and $\bar{G}(\lambda,h)$, $\bar{F}$ is related to the probability of inserting a cavity by use of the general result of fluctuation theory [25],

$$W(\lambda,h) = -kT\ln P_0(\lambda,h), \tag{8}$$

where $P_0(\lambda,h)$ is the probability of randomly observing the desired cavity configuration. Substituting the above into Eq. (6) and differentiating with respect to h yields

$$\bar{F}(\lambda,h) = \frac{-1}{2\pi\rho\lambda^2}\frac{\partial \ln P_0(\lambda,h)}{\partial h}. \tag{9}$$

For all cavity sizes, P_0 may be expressed in terms of second-order, third-order, etc., correlation functions [3]. Since these functions are not known in general, this expression for P_0 is of limited applicability. Yet, for certain values of h for a given λ, P_0 reduces to a form that yields an exact and useful relation for $\bar{F}(\lambda,h)$.

A. Exact expression for $\bar{F}(\lambda,h)$

For cavities that intersect the plane at $z=0$ and may contain at most one hard-sphere center, P_0 is rigorously given by [1]

$$P_0(\lambda,h) = 1 - \pi\int_0^{h+\lambda} \rho(z)[\lambda^2-(z-h)^2]dz, \tag{10}$$

where $\rho(z)$ is the aforementioned density of hard-sphere centers at z. By integrating the density profile over a body of revolution corresponding to that portion of the cavity beyond $z=0$, the second term on the right-hand side of Eq. (10) determines the average number of hard-sphere centers found within the cavity. When this number is subtracted from unity, given that the cavity can contain at most one particle center, the result is simply $P_0(\lambda,h)$. In Ref. [1], Eq. (10) was shown to be valid for cavities whose largest chord spanned a distance equal to σ (again ensuring that the cavity could contain at most one hard-sphere center). Presently, this condition is satisfied by one of two different criteria:

(1) For $\lambda\leq\sigma/2$ and all cavity centers for which $-\lambda\leq h\leq\lambda$.

(2) For $\lambda>\sigma/2$ and all cavity centers for which $-\lambda\leq h\leq-\sqrt{\lambda^2-(\sigma/2)^2}$.

Entering Eq. (10) into Eq. (9) results in the following *exact* expression for $\bar{F}(\lambda,h)$:

$$\bar{F}(\lambda,h) = \frac{\displaystyle\int_0^{h+\lambda}\rho(z)(z-h)dz}{\rho\lambda^2\left(1-\pi\displaystyle\int_0^{h+\lambda}\rho(z)[\lambda^2-(z-h)^2]dz\right)}, \tag{11}$$

for the criteria listed above. The above relation confirms that $\bar{F}(\lambda,-\lambda)=0$, since the force on a cavity with no exposed surface area should vanish. Taking the derivative of Eq. (11) with respect to h also shows that the slope of $\bar{F}(\lambda,h)$ at $h=-\lambda$ is positive. This result is consistent with the arguments presented in the preceding section, where we noted that $\bar{F}(\lambda,h)$ should be positive for $h\leq0$.

Another thermodynamic consistency check of $\bar{F}(\lambda,h)$ is available for the limit of $h\to-\lambda$. Since the fluid exerts a stress on the $z=0$ plane equal to the bulk fluid pressure when the cavity is absent, the limiting stress on the cavity surface in the z direction, just as the cavity is being pushed into the fluid, should also be identical to the bulk fluid pressure [9–11]. Hence, the force in the (negative) z direction divided by the surface area projected in the z direction must equal p as the cavity vanishes beyond the $z=0$ plane, or

$$\lim_{h\to-\lambda}\frac{-F(\lambda,h)}{A_p(\lambda,h)} = p, \tag{12}$$

where $A_p(\lambda,h)=\pi(\lambda^2-h^2)$ is the surface area of the cavity projected onto the $z=0$ plane. When rewritten using $\bar{F}(\lambda,h)$ and Eq. (6), the expected limit becomes

$$\lim_{h\to-\lambda}\left(\frac{2\lambda^2}{\lambda^2-h^2}\bar{F}(\lambda,h)\right) = \frac{p}{\rho kT}. \tag{13}$$

Upon entering Eq. (11) into the above, one finds that

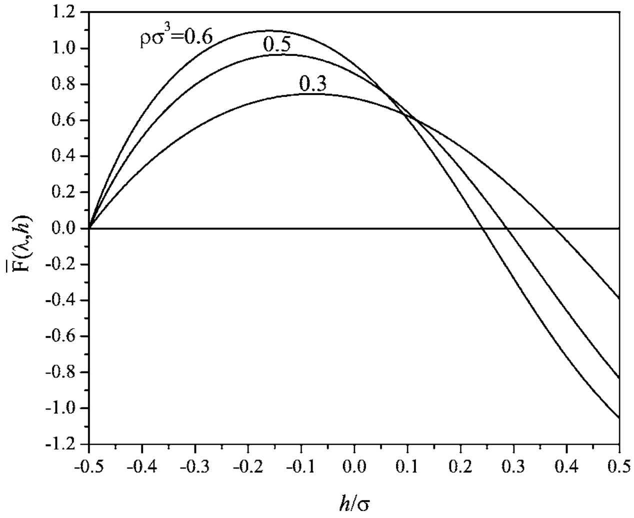

FIG. 2. $\bar{F}(\lambda,h)$ plotted for $\lambda=\sigma/2$ and $\rho\sigma^3=0.3$, 0.5, and 0.6. Positive values of $\bar{F}(\lambda,h)$ indicate that the force exerted by the solvent on the cavity is directed toward the wall (attraction), negative values indicate that the cavity is pulled away from the wall (repulsion). Note that each maximum occurs for $h<0$, i.e., before the cavity is hemispherical at $h=0$. Beyond $h=\sigma/2$, the cavity no longer intersects the $z=0$ plane.

$$\lim_{h\to-\lambda}\left(\frac{2\lambda^2}{\lambda^2-h^2}\bar{F}(\lambda,h)\right)=\frac{\rho(0)}{\rho}, \tag{14}$$

which is indeed $p/\rho kT$ since $\rho(0)=p/kT$.

Since the form of $\bar{F}(\lambda,h)$ within the exact domain has some bearing on how $\bar{F}(\lambda,h)$ is later approximated beyond this limit, we first present $\bar{F}(\lambda,h)$ and $W(\lambda,h)$ for $\lambda\leqslant\sigma/2$ using density profiles, $\rho(z)$, obtained from MC simulations. Figure 2 shows $\bar{F}(\lambda,h)$ calculated from Eq. (11) for $\lambda=\sigma/2$ and bulk densities of $\rho\sigma^3=0.3$, 0.5, and 0.6 (a cavity of radius $\lambda=\sigma/2$ is equivalent to a point particle). For this cavity radius, overlap with the $z=0$ plane occurs for $-\sigma/2\leqslant h\leqslant\sigma/2$. As expected, $\bar{F}$ begins at zero and is positive for all $h<0$, corresponding to $\theta<\pi/2$. Also as anticipated, the net force on the cavity vanishes at a sufficiently large $h>0$ (when θ may exceed $\pi/2$), with $\bar{F}<0$ at larger values of h. This negative force, physically interpreted as the cavity being "pulled" further into the fluid or "pushed" away from the wall, confirms that a repulsive depletion force does develop between a point particle and a flat wall. [Note that $\bar{F}(\lambda,h)$ is proportional to $F(\lambda,h)$, but with an opposite sign, where $F(\lambda,h)$ is the total force exerted on the cavity in the negative z direction.] Interestingly, a nontrivial repulsive barrier develops that could prevent a point particle from being "deposited" at the hard wall. Figure 2 also reveals that the value of $h>0$ at which the force is zero decreases with density, while the maximum value of $\bar{F}$ always appears for $h<0$, i.e., before particle centers are able to exert a force on the cavity in the positive z direction. The latter is a somewhat unexpected result, since the total force on the cavity was presumed to decrease only after $h>0$, when particles are able to access locations for $\theta>\pi/2$ and counteract the force exerted by particles situated at $\theta<\pi/2$. An explanation of the location of the maximum in $\bar{F}$ is postponed until Sec. VII. We also note that similar $\bar{F}$ profiles are observed for $\lambda<\sigma/2$.

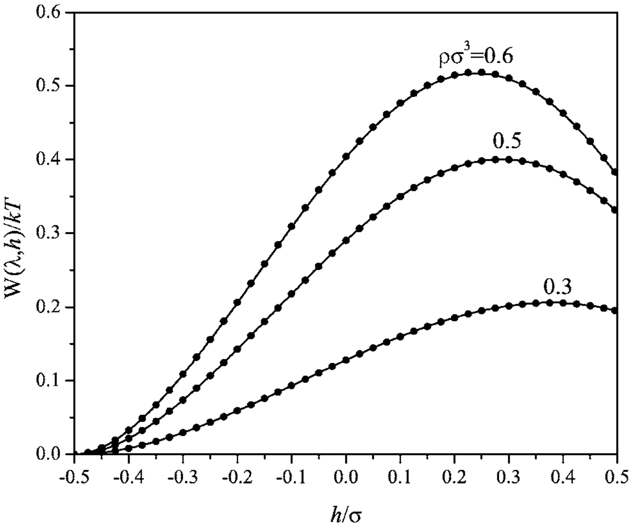

FIG. 3. Reversible work of cavity insertion, $W(\lambda,h)$, calculated for $\lambda=\sigma/2$ and $\rho\sigma^3=0.3$, 0.5, and 0.6. The solid lines are the I-SPT predictions generated by integrating $\bar{F}(\lambda,h)$ in Fig. 2. The solid circles represent Monte Carlo simulation results.

Finally, in Fig. 3, we present $W(\lambda,h)$ obtained from each of the $\bar{F}(\lambda,h)$ profiles displayed in Fig. 2, along with the corresponding work predictions obtained by molecular simulation (see Sec. IV for details). As expected, excellent agreement between the theoretical results and the simulation predictions for the entire h domain is obtained (differences in work values did not exceed $2\times10^{-3}kT$). Since $\bar{F}$ changes sign, the slope of W also changes sign, in which the location of the maximum of W corresponds, of course, to the value of h at which $\bar{F}=0$.

B. Interpolation scheme for $\bar{F}(\lambda,h)$

When the cavity is pushed into the fluid such that its largest chord exceeds σ (which occurs only for $\lambda>\sigma/2$), Eq. (11) is no longer valid. Beyond this point, as in other versions of SPT, we approximate $\bar{F}(\lambda,h)$ with an interpolation function that incorporates exact information generated from both thermodynamic and geometric arguments. In what follows, we first identify various conditions on $\bar{F}$ and then propose interpolation polynomials that incorporate this information.

1. *Geometric conditions*

A number of conditions on $\bar{F}$ are dictated by geometry. Although Eq. (11) is no longer valid for $h>-\sqrt{\lambda^2-(\sigma/2)^2}$ when $\lambda>\sigma/2$, we show in Appendix A that $\bar{F}(\lambda,h)$ and its first derivative with respect to h are continuous at $h=-\sqrt{\lambda^2-(\sigma/2)^2}$, providing two exact conditions on $\bar{F}$ [analogous to the two continuity conditions on $G(\lambda)$ and $\bar{G}(\lambda,h)$ [1]]. We also demonstrate in Appendix A that $\partial^2\bar{F}/\partial h^2 \to -\infty$ as $h \to -\sqrt{\lambda^2-(\sigma/2)^2}$ from above. Enforcement of this additional exact condition does not appear to be necessary, and so is not included in the interpolation scheme discussed below.

A third condition is available from our previous version of I-SPT for hemispherical cavities [1]. Because the reversible work of cavity formation is path independent, the work of "growing" a hemispherical cavity of radius λ at $h=0$ must equal the work of "pushing" a cavity at fixed radius λ to $h=0$. Hence, using Eqs. (2) and (7), we require that

$$\lambda^2\int_{-\lambda}^{0}\bar{F}(\lambda,z)dz = \int_{0}^{\lambda}\bar{G}(r)r^2dr. \tag{15}$$

The above is a formally *exact* integral condition on $\bar{F}$. $\bar{G}(\lambda)$ is not known exactly beyond $\lambda=\sigma/2$, however, so the application of Eq. (15) relies upon the accuracy of the chosen interpolation of $\bar{G}(\lambda)$. Reference [1] showed that the work predictions obtained by representing $\bar{G}(\lambda)$ via a simple interpolation function were very accurate up to moderate bulk densities, but deviated somewhat from simulation results at high densities ($\rho\sigma^3 \gtrsim 0.9$). Appendix A describes a needed modification to the interpolation scheme for $\bar{G}(\lambda)$ that improves the predictions of the hemispherical work function at high density. With this interpolation, we may consider Eq. (15) to be, in practice, *nearly exact* for all densities. (Similar to $\bar{F}$, we show in Appendix A that $\partial^2\bar{G}/\partial\lambda^2$ is divergent for $\lambda \to \sigma/2$ from above, a result speculated upon, but not proven, in Ref. [1]. Unlike $\bar{F}$, however, incorporating the divergence of $\partial^2\bar{G}/\partial\lambda^2$ into an interpolation scheme is crucial for improving the predictions of the work of growing hemispherical cavities at high densities.)

2. Thermodynamic conditions

The above geometric conditions constrain the form of $\bar{F}$ only for $h \leqslant 0$. In light of Fig. 2, where $\bar{F}$ is shown to be a nonmonotonic function of h, conditions for $h>0$ are required if $\bar{F}$ is to be predicted with sufficient accuracy up to $h=\lambda$. Preliminary investigations revealed that information about $\bar{F}$ is particularly needed for $\lambda-\sigma \leqslant h \leqslant \lambda$, a range of h spanning both positive and negative values of $\bar{F}$. Note that $h=\lambda-\sigma$ corresponds to the distance at which the surface of the equivalent solute contacts the hard wall (located at $z=-\sigma/2$) and represents a physically relevant configuration, while $h=\lambda$ corresponds to the distance at which the cavity no longer intersects the $z=0$ plane. Most importantly, the interpolation of $\bar{F}$ required a condition that located the value of $h>0$ where $\bar{F}$ vanishes, or $\bar{F}(\lambda,h)=0$.

Although $\bar{F}$ is not known in general for $h>0$, all values of $\bar{F}$ between $\lambda-\sigma \leqslant h \leqslant \lambda$ can be determined from the density profile, $\rho(z)$, for $\lambda=\sigma$, when the cavity is equivalent to another hard-sphere solvent particle. Since the potential-distribution theory of Widom requires that [26,27]

$$\frac{\rho(z)}{\rho} = \exp\left(-\frac{[W(\sigma,h=z)-W(\sigma,h\to\infty)]}{kT}\right), \tag{16}$$

we find with Eq. (7) that

$$\bar{F}(\sigma,h) = -\frac{1}{2\pi\rho\sigma^2}\left.\frac{d\ln\rho(z)}{dz}\right|_{z=h}. \tag{17}$$

In addition, information about $\bar{F}$ can be obtained in the limit of $\lambda\to\infty$. For example, if we introduce the following three functions:

$$f_{c1}(\lambda) = \lambda\bar{F}(\lambda,\lambda-\sigma), \tag{18}$$

$$f_{c2}(\lambda) = \lambda - h_0(\lambda), \tag{19}$$

where $h_0(\lambda)$ is defined such that $\bar{F}(\lambda,h_0(\lambda))=0$, and

$$f_{c3}(\lambda) = \lambda\bar{F}(\lambda,\lambda), \tag{20}$$

we show in Appendix B that each of the above approaches an asymptotic value given by

$$f_{c1}(\infty) = \frac{p\sigma+2\gamma_\infty}{\rho kT}, \tag{21}$$

$$f_{c2}(\infty) = \frac{-2\gamma_\infty}{p}, \tag{22}$$

$$f_{c3}(\infty) = \frac{2\gamma_\infty}{\rho kT}, \tag{23}$$

in which γ_∞ is the planar surface (or more properly the boundary) tension of the hard-sphere fluid [3]. Since $\gamma_\infty<0$, $f_{c3}(\infty)$ is negative, indicating a net repulsive force on a cavity centered at $h=\lambda$ in the limit of infinite radius. The sign of $f_{c1}(\infty)$ is not as readily apparent. Using the pressure p from the Carnahan-Starling equation of state (CS-EOS)[28] and an expression for γ_∞ that is consistent with the CS-EOS (see Refs. [22,29]), we find that $f_{c1}(\infty)>0$ for all fluid densities below the hard-sphere freezing transition ($\rho\sigma^3<0.943$ [30–32]). Hence, the force on a cavity or equivalent solute centered at h=$\lambda-\sigma$ is always attractive in the infinite limit. The opposite signs of $f_{c1}(\infty)$ and $f_{c3}(\infty)$ are also consistent with the positive values obtained for $f_{c2}(\infty)$. Again using p and γ_∞ for the CS-EOS, we find that $0<f_{c2}(\infty)<\sigma$ for all densities below the freezing transition, implying that $\lambda-\sigma<h_0(\infty)<\lambda$. Thus, in the limit as the solute becomes of macroscopic size, the force on the solute vanishes (i.e., the depletion force is zero) for a surface to wall separation that is always less than σ (which follows from the force being attractive at $h=\lambda-\sigma$ and repulsive at $h=\lambda$). Interestingly, $-2\gamma_\infty/p$ emerges as a relevant length scale for this inhomogeneous system.

The values of f_{c1}, f_{c2} and f_{c3} can also be determined for $\lambda=\sigma$ via Eq. (17), where, for example, f_{c2} corresponds to the first minimum of $\rho(z)$. Except for a specific range of small cavity radii, these functions are not known at other (finite) values of λ. To generate information in between these known radii, thereby obtaining needed conditions on $\bar{F}$ at any chosen λ, we represent each f_{ci} by the following asymptotic function:

$$f_{ci}(\lambda) = \psi_{0i}(\rho) + \frac{\psi_{1i}(\rho)}{\lambda} + \frac{\psi_{2i}(\rho)}{\lambda^2} + \frac{\psi_{3i}(\rho)}{\lambda^3}. \tag{24}$$

The fitting coefficients $\psi_{ji}(\rho)$ are determined from knowledge of f_{ci} at $\lambda=\sigma$ and $\lambda\to\infty$, and from the *exact* value of the function and its first derivative at either $\lambda=5\sigma/8$ for f_{c1} or $\lambda=\sigma/2$ for both f_{c2} and f_{c3} (see Appendix B). As shown in Appendix B, simulation results for f_{ci} are in very good agreement with Eq. (24). While f_{c1} and f_{c2} always increase toward their asymptotic values, f_{c3} exhibits interesting behavior at high density. For $\rho\sigma^3 \gtrsim 0.8$, f_{c3} does not remain negative for all λ. At these densities, f_{c3}, after starting off negative, begins to increase until it becomes positive around $\lambda=\sigma$, before finally becoming negative again as it approaches its asymptotic value of $f_{c3}(\infty) < 0$. Consequently, the force on a cavity of radius $\lambda\sim\sigma$ centered at $h=\lambda$ will be attractive, instead of repulsive, at these high densities. Since f_{c1} is always positive (attractive force at contact with the wall), and an intermediate repulsive interval is still exhibited, solutes with cavity radii around σ exhibit at these high densities two locations at which the force acting upon them vanishes. The origin of this high density behavior stems from the appearance of another point of zero force in the solvent density profile, $\rho(z)$, where a maximum develops before $z=\sigma$ [which translates to a positive slope for f_{c3} at the exact limit of $\lambda=\sigma/2$ along with $f_{c3}(\sigma)>0$, as required by Eq. (17)]. Note that f_{c2} only describes the location of the minimum, and not the subsequent maximum, and so is unaware of the second vanishing of $\bar{F}$. Our chosen representation of f_{c3} is very accurate for low to moderate densities for $\lambda=\sigma/2$ to $\lambda\sim\sigma$ and for large cavity sizes at all densities, but becomes less accurate at high densities for those intermediate cavity radii over which f_{c3} becomes positive (see Appendix B). Nevertheless, our later interpolation of $\bar{F}$ is ensured to be highly accurate if we focus on lower densities and/or large solutes (as in the colloidal limit), where f_{c3} is either always negative or very close to its asymptotic value, respectively (where the behavior of f_{c3} at intermediate cavity radii is irrelevant).

With the above three functions, f_{ci}, we may now add three more conditions on $\bar{F}(\lambda,h)$. These conditions, however, are not the only conditions that could be generated for $\lambda-\sigma \leq h \leq \lambda$. In fact, we could introduce other functions f_{ci} that incorporate information about $\bar{F}$ again at $\lambda=\sigma$, via Eq. (17), and $\lambda\to\infty$ (see Appendix B) for $\lambda-\sigma \geq h \geq \lambda$. The selection of $h=\lambda-\sigma$, where the cavity is equivalent to a solute in contact with the wall, $h=\lambda$, where the cavity no longer intersects the $z=0$ plane, and $h_0(\lambda)$, the location at which the force vanishes, provide conditions on $\bar{F}$ at values of h that were found to be particularly important. Other conditions may be incorporated, but this serves to increase the complexity of the interpolation scheme used to represent $\bar{F}$ without generating significantly more accurate results. It is also possible that replacing the three chosen values of h with three others within $\lambda-\sigma \leq h \leq \lambda$ may lead to acceptable predictions of $\bar{F}$, a route we did not explore in great detail.

C. Interpolation scheme

The exact plots of $\bar{F}(\lambda,h)$ in Fig. 2 suggest that $\bar{F}(\lambda,h)$ beyond the exact limit may be well approximated by a polynomial, instead of an asymptotic series, that incorporates a number of exact or pseudoexact conditions. Since we currently have six conditions on $\bar{F}$, as provided in the preceding two sections, we first attempted to represent $\bar{F}$ by a single sixth-order polynomial in h. This interpolation polynomial could not, however, adequately describe the shape of $\bar{F}$ over the entire h domain for a wide range of cavity radii and fluid densities. We then considered representing $\bar{F}$ by two separate polynomials linked together at a well-chosen value of h. The interpolation scheme we ultimately selected for $\lambda \geq \sigma$ approximates $\bar{F}(\lambda,h)$ by

$$\bar{F}(\lambda,h) = \begin{cases} \alpha_{10}(\rho,\lambda) + \alpha_{11}(\rho,\lambda)h + \alpha_{12}(\rho,\lambda)h^2 + \alpha_{13}(\rho,\lambda)h^3 & -\sqrt{\lambda^2 - \left(\frac{\sigma}{2}\right)^2} < h \leq \lambda - \sigma, \\ \alpha_{20}(\rho,\lambda) + \alpha_{21}(\rho,\lambda)h + \alpha_{22}(\rho,\lambda)h^2 + \alpha_{23}(\rho,\lambda)h^3 & \lambda - \sigma < h \leq \lambda, \end{cases} \tag{25}$$

in which $\alpha_{ij}(\rho,\lambda)$ are the adjustable parameters of the interpolation, with i identifying the interpolation polynomial (1 or 2) and j indicating that the coefficient is multiplied by h^j. The two polynomials are joined at $h=\lambda-\sigma$, a position where a matching condition fixes $\bar{F}$ (see the preceding section). Although arbitrary, this particular h value was chosen since it corresponds to the first physical location of the corresponding solute (whose surface is in contact with the wall) and led to good agreement with simulation results when $\lambda \geq \sigma$. Linking the two polynomials at $h=\lambda-\sigma$ when $\lambda<\sigma$ (so that $h=\lambda-\sigma<0$) did not yield an overall good representation of $\bar{F}(\lambda,h)$ for these small cavities. In this case, the two polynomials were instead linked at $h=0$ (leading to much better agreement with simulation results). In what follows, we focus our attention on cavities for which $\lambda \geq \sigma$, and only consider results obtained with Eq. (25).

The eight fitting coefficients appearing in Eq. (25) are obtained by imposing the six matching conditions discussed in the preceding subsections, along with two conditions of continuity at $h=\lambda-\sigma$. As a review, the six geometric and thermodynamic constraints are

(1) $\bar{F}(\lambda,-\sqrt{\lambda^2-(\sigma/2)^2})$ computed exactly by Eq. (11)

(2) $\partial\bar{F}/\partial h|_{h=-\sqrt{\lambda^2-(\sigma/2)^2}}$ computed exactly by a derivative of Eq. (11) with respect to h,

(3) $\lambda^2\int_{-\lambda}^{0}\bar{F}(\lambda,z)dz=\int_0^{\lambda}\bar{G}(r)r^2dr$

(4) $\bar{F}(\lambda,\lambda-\sigma)=f_{c1}(\lambda)/\lambda$,

(5) $\bar{F}[\lambda,\lambda-f_{c2}(\lambda)]=0$,

(6) $\bar{F}(\lambda,\lambda)=f_{c3}(\lambda)/\lambda$.

In addition, we also require that $\bar{F}$ and $\partial\bar{F}/\partial h$ be continuous across $h=\lambda-\sigma$, the point where the two polynomials are linked together. [The continuity of $\bar{F}$ at $h=\lambda-\sigma$ is implied by condition 4, which is invoked separately by each fitting polynomial.] Hence, the final two conditions on $\bar{F}$ are

(7) $\bar{F}(\lambda,h)$ is continuous at $h=\lambda-\sigma$ [required by condition (4)],

(8) $\partial\bar{F}/\partial h$ is continuous at $h=\lambda-\sigma$.

With eight matching conditions identified, each α_{ij} can now be obtained by straightforward solution of the resulting linear equations. By entering the resulting interpolation polynomials for $\bar{F}(\lambda,h)$ into Eq. (7), we can then calculate $W(\lambda,h)$. In the following sections, we present the results of our chosen interpolation scheme for $\lambda\geqslant\sigma$ at various fluid densities, and compare them to molecular simulation predictions.

IV. SIMULATION METHOD

The comparison of our I-SPT predictions of $W(\lambda,h)$ with simulation results requires that both $W(\lambda,h)$ and $\rho(z)$ be determined computationally. (Although analytic approximations for the density profile of a hard-sphere solvent at a hard wall are available in the literature, e.g., Refs. [33,34], these approximations show significant deviations from simulation at moderate to high packing fractions. Thus, to eliminate this potential source of error in our theory, we chose to use density profiles generated by simulation.) All simulations were performed using a Monte Carlo (MC) algorithm for the isothermal-isobaric (constant N, p, T) ensemble with hard walls [35,36]. All variables were scaled using the characteristic values for hard sphere systems. Hard walls were imposed at the z limits of the simulation cell and periodic boundary conditions were applied in the x and y directions. The number of particles used in each simulation was adjusted to ensure that a uniform fluid phase with the appropriate bulk properties developed in the center of the simulation cell, ranging from 500 to 3000 depending on the chosen pressure. Each simulation was run for a target density in the center of the simulation cell, with the imposed pressure being calculated from the CS-EOS to ensure consistency between the interior density ρ, the density profile, $\rho(z)$, and the wall contact density $\rho(0)=p/kT$. The x and y dimensions of the simulation cell were chosen large enough to prevent a cavity from "sensing" its periodic image. As a rule of thumb, these dimensions were at least $4\lambda_{\max}$, where $\lambda_{\max}$ is the largest cavity radius probed by the simulation. The simulations were allowed to equilibrate before recording results for a sufficient number of cycles, typically 3×10^4 to 10^5, where each cycle included N particle translations and one volume adjustment. Volume moves were accomplished by adjusting only the length of the simulation cell in the z direction [35,36] and accepted according to standard NpT acceptance criteria [37], while translational moves were accomplished by randomly moving particles and looking for particle overlap. Simulation density profiles were generated by measuring the local density as a function of z and averaging each z bin over the length of the simulation. Results were collected over a production run of 10^6 to 5×10^6 cycles.

The reversible work of cavity formation for different λ and h was calculated from the probability of observing cavities along the hard wall. A point along the wall was randomly selected and the corresponding h positions for cavities of a given radius λ were determined. To determine $W(\lambda,h)$ for large cavity sizes (generally $\lambda>1.5\sigma$), an umbrella sampling technique [37] was employed in which windows of progressively larger values of h, for a given fixed cavity radius were probed. An additional MC step was added, in which the cavity was allowed to change its z coordinate, on average, once per MC cycle. The translation of the cavity was controlled according to a biasing potential, $\psi(h)$. Good statistics are achieved when $\psi(h)=-W(\lambda,h)$, so a third-order polynomial regression of the previously collected cavity work profile was used to extrapolate $\psi(h)$ into the next window [38]. After completing a window, the probability histogram was normalized according to the biasing potential and linked with the previously collected work data to obtain the updated cavity work profile. With this method, work profiles for cavity radii around 3σ (or less) were obtained. Determination of $W(\lambda,h)$ beyond these sizes, at least for moderate to high densities, becomes too computationally expensive because of the large system sizes and number of windows required.

V. INTERPOLATED RESULTS

Once the density profile, $\rho(z)$, and bulk pressure are known, both $\bar{F}(\lambda,h)$ and $W(\lambda,h)$ for $\lambda\geqslant\sigma$ can be determined for $-\lambda\leqslant h\leqslant\lambda$ by combining the exact results over $-\lambda\leqslant h\leqslant-\sqrt{\lambda^2-(\sigma/2)^2}$ (see Eq. (11)) with the interpolated values of $\bar{F}(\lambda,h)$ obtained from Eq. (25). Since we are comparing our predictions to the results of NpT MC simulations based upon the pressure of the CS-EOS, all matching conditions that require an equation of state and an expression for γ_∞ are also based on the CS-EOS. [The previous I-SPT interpolation for $\bar{G}(\lambda)$ [1] was based on a thermodynamically consistent adaptation of SPT to the CS-EOS (labelled CS-SPT) [22], which yielded a prediction of γ_∞ that was not in agreement with the simulation results of Refs. [39,40]. Since then a modified form of CS-SPT has been developed by us [29] that now generates values of γ_∞ in excellent agreement with simulation results and the semiempirical expression of Henderson and Plischke [41]. Here, we make use of γ_∞ obtained from our modified version of CS-SPT.]

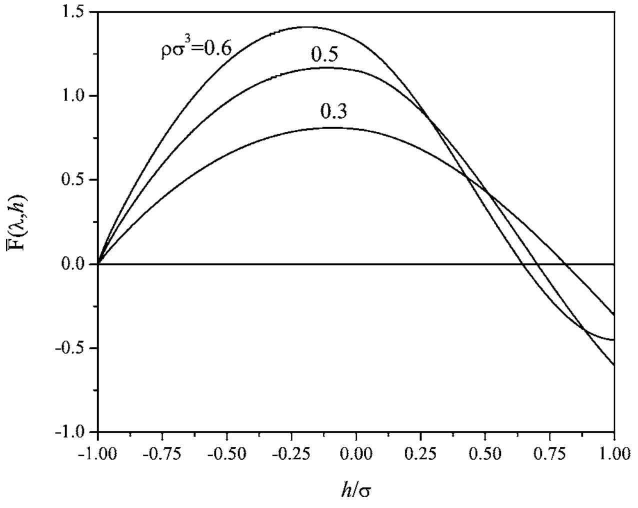

FIG. 4. $\bar{F}(\lambda,h)$ versus h for $\lambda=\sigma$ and $\rho\sigma^3=0.3$, 0.5, and 0.6. $\bar{F}$ is known exactly for $-1\leqslant h/\sigma\leqslant-\sqrt{3}/2$.

To begin, we present our predictions of $\bar{F}$ and W for $\lambda=\sigma$, when the cavity is equivalent to a hard-sphere solvent particle, in which both are known exactly for $-\sigma\leqslant h\leqslant-\sqrt{3}\sigma/2$. $\bar{F}(\lambda,h)$ is provided in Fig. 4 for the bulk densities $\rho\sigma^3=0.3$, 0.5, and 0.6. As imposed by the interpolation, $\bar{F}$ exhibits a maximum at $h<0$ and equals zero at some positive value of h, becoming negative thereafter. The absolute value of $\bar{F}$ increases (not linearly) with an increase in density only for $h<0$ and for locations close to $h=\sigma$. For values of h around 0.5σ, $\bar{F}$ exhibits more complicated behavior with respect to changes in density. The corresponding $W(\lambda,h)$ profiles obtained from each $\bar{F}$ given in Fig. 4 is provided in Fig. 5. The I-SPT predictions of W agree quite well with the simulation results, although there are some minor differences at $\rho\sigma^3=0.6$ in the vicinity of the maximum of W. Nevertheless, the maximum deviation between theory and simulation is about $0.14kT$, a difference of only 2.5%. This small error can be attributed to the interpolation scheme, since we have imposed, via $\rho(z)$, three exact matching conditions on $\bar{F}$ based on formally exact knowledge of a cavity with $\lambda=\sigma$. Although our predictions of W are quite accurate, we may still conclude that our chosen interpolation polynomials do not truly describe the correct behavior of $\bar{F}$ over all relevant values of h. (Figure 5 and later plots do indicate that the first polynomial over $h\leqslant\lambda-\sigma$ provides a highly accurate representation of $\bar{F}$ as long as $h=\lambda-\sigma$ is not too close to the maximum in W. In fact, the largest deviations between I-SPT and simulation always arises around this maximum, which suggests that a single polynomial beyond $h=\lambda-\sigma$, though still good for our present purposes, does not completely capture the somewhat more complicated behavior of $\bar{F}$ in this region. One straightforward modification, which we did not investigate, is to add a third polynomial, such that two fitting polynomials are utilized between $\lambda-\sigma\leqslant h\leqslant\lambda$. Additional matching conditions can be generated by introducing more of the functions f_{ci}, which are known exactly over $\lambda-\sigma\leqslant h\leqslant\lambda$ for small cavity radii, $\lambda=\sigma$ and $\lambda\rightarrow\infty$.)

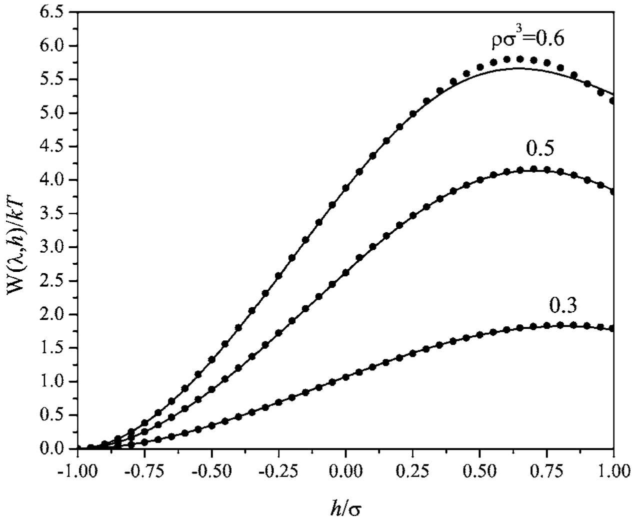

FIG. 5. Reversible work of cavity insertion, $W(\lambda,h)$, versus h, for $\lambda=\sigma$ calculated from $\bar{F}(\lambda,h)$ provided in Fig. 4. Solid lines represent the I-SPT predictions, while the solid circles are the MC simulation results.

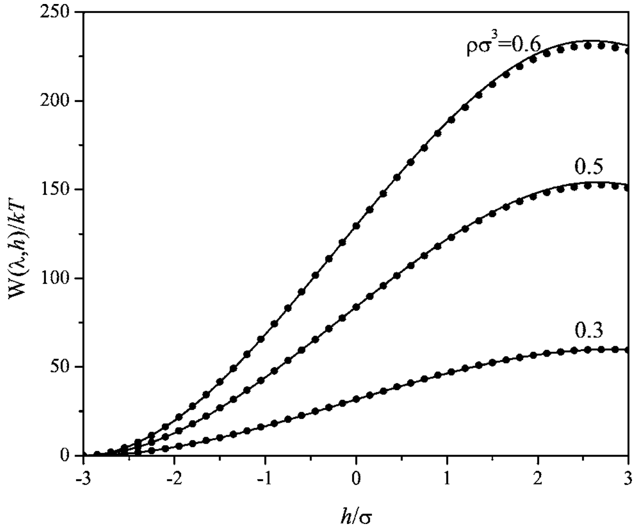

FIG. 6. Reversible work of cavity insertion, $W(\lambda,h)$, versus h for $\lambda=3\sigma$ and the same densities shown in Fig. 4. Solid lines represent the I-SPT predictions, while the solid circles are the MC simulation results.

To examine the accuracy of the $\bar{F}$ interpolation for larger λ, we compare in Fig. 6 the I-SPT and simulation predictions of W for $\lambda=3\sigma$ and the same densities shown in Fig. 5. Here, $\bar{F}$ and W are known exactly only for $-3\sigma\leqslant h\leqslant-2.96\sigma$, a much smaller interval than for $\lambda=\sigma$. Nevertheless, W obtained from I-SPT is in excellent agreement with simulation over the entire range of h (even around the maxima). The largest error observed is only $3.1kT$, a difference of 1.3%. In light of Fig. 4, the improvement of the work predictions, particularly around the maxima, as the cavity radius was increased suggests that the interpolation of $\bar{F}$ yields more accurate results at larger radii. The improved accuracy of $\bar{F}$ is also encouraging, given that domain of h over which $\bar{F}$ is

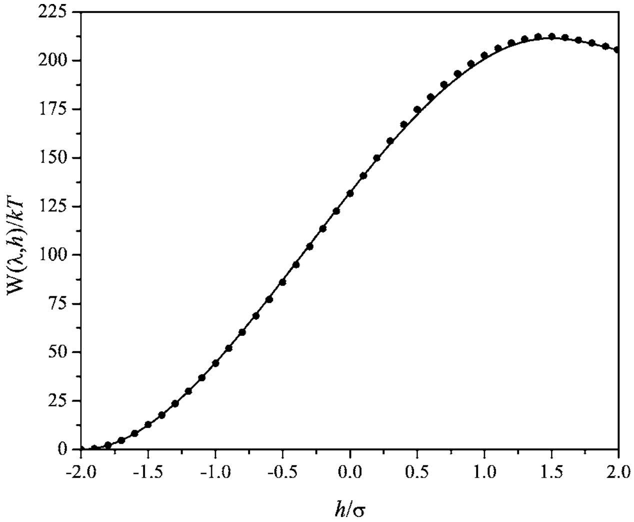

FIG. 7. Reversible work of cavity insertion, $W(\lambda,h)$, versus h for $\lambda=2\sigma$ and $\rho\sigma^3=0.914$. The solid line represents the I-SPT predictions, while the solid circles are the MC simulation results.

known exactly has become quite small. Consequently, the representation of $\bar{F}$ relies primarily on the chosen interpolation between the imposed matching conditions on $\bar{F}$, and yet still yields a highly accurate prediction of the work of cavity insertion.

Finally, we provide a more rigorous test of our I-SPT predictions in Fig. 7, which displays W for $\lambda=2\sigma$ and $\rho\sigma^3=0.914$, a density very near to the freezing transition. At this high density, $f_{c3}(\sigma)$ is positive rather than negative, which modifies the shape of $\bar{F}$ near $h=\lambda$, as compared to the previous lower density examples. Nevertheless, the agreement between I-SPT predictions and simulation is still very good. The largest observed difference is about $2.7kT$, which compared to the work of insertion around $172kT$ corresponds to a fractional error of only 1.6%. Overall, our chosen interpolation scheme describing $\bar{F}$ is quite robust, yielding accurate predictions of W up to high densities and a wide range of cavity radii.

VI. DEPLETION FORCE CALCULATION BY I-SPT

Given an expression for $\bar{F}$, the depletion, or entropic, force between a hard-sphere colloid and a wall can be straightforwardly determined for separation distances inclusive of $h=\lambda-\sigma$, when the colloid is in contact with the wall, and $h=\lambda$, when the equivalent cavity of the solute no longer intersects the $z=0$ plane. If the hard-sphere diameter of the solute is σ_s, the equivalent cavity is, as mentioned before, $\lambda=(\sigma_s+\sigma)/2$. As a simplification, we define a distance parameter, $z^*=h-\lambda+\sigma$, which denotes the distance between the actual hard wall and the surface of the hard-sphere solute, where $0\leqslant z^*\leqslant\sigma$. In terms of σ_s, z^* and the I-SPT function $\bar{F}$, the force, $F(z^*)$, on the solute is equal to [see Eq. (6)]

$$F(z^*) = -2\pi\rho kT\left(\frac{\sigma_s+\sigma}{2}\right)^2\bar{F}\left(\frac{\sigma_s+\sigma}{2}, z^*-\frac{\sigma_s-\sigma}{2}\right), \tag{26}$$

in which $\bar{F}$ is computed in the same manner as discussed before.

Figures 8 and 9 display the I-SPT predictions for the entropic force between a hard-sphere colloid and a wall for diameters of $\sigma_s=5\sigma$ and $\sigma_s=10\sigma$, respectively, for packing fractions $\eta=0.1$, 0.2, 0.3, and 0.4 ($\eta=\pi\rho\sigma^3/6$). Both figures compare the I-SPT results to the MC simulation results of Dickman *et al.* [24] and depletion force predictions obtained using the bulk SPT-based method introduced previously by Corti and Reiss [18]. Also included are the forces calculated using the Asakura-Oosawa (AO) approximation [4], which is a limiting case of our method and can be obtained by setting $G(\lambda,\theta,h)=1$ in Eq. (5). As can be seen in the figures, the AO approximation always yields a negative entropic force that vanishes at $z^*=\sigma$. As anticipated from our previous discussions of the behavior of $\bar{F}(\lambda,h)$, the depletion force is initially negative (attractive) and then becomes positive (repulsive) as z^* nears σ. The agreement between the I-SPT predictions and the MC simulation data of Dickman *et al.* [24] is excellent, particularly for $\sigma_s=5\sigma$. Some discrepancies appear at $\sigma_s=10\sigma$, though our predictions may still lie within the error bars of the simulation results. The I-SPT results are quite consistent with the bulk SPT-based method for $\eta\leqslant0.2$, though the SPT approach begins to overpredict $F(z^*)$ for $z^*\to\sigma$ at higher densities. Unlike the SPT-based method, I-SPT is aware of the high density appearance of a second attractive regime at intermediate solute diameters, which serves to decrease the repulsive force for larger solutes (see Appendix B). (We do note, though, that as $\lambda\to\infty$ the two methods recover identical asymptotic limits.) The vast improvement seen for $\eta=0.3$ and, presumably, $\eta=0.4$ demonstrates the advantage that I-SPT has over the bulk SPT method. This confirms that the line tension of the three-phase (cavity-wall-solvent) interface is a quantity that cannot be overlooked, especially in the vicinity of $z^*\approx\sigma$ and at high packing fractions.

We conclude this section by considering the depletion forces that develop for $\sigma_s/\sigma\sim1$ at high solvent densities. As discussed previously and in Appendix B, f_{c3}, and therefore F, becomes positive for $0.64\sigma<\lambda<1.37\sigma$ at $\rho\sigma^3=0.914$. Consequently, the depletion force again becomes attractive at $z^*=\sigma$ for colloidal diameters within $0.28\sigma\leqslant\sigma_s\leqslant1.74\sigma$, exhibiting two values of $z^*<\sigma$ at which the entropic force vanishes. Although the full force profile is known to exhibit oscillations between negative and positive values of F (e.g., Ref. [24]), attention has focused on large solutes where F vanishes for a second time only for $z^*>\sigma$. Here we see at high densities and small solute diameters that the full force profile oscillates more rapidly than at lower densities and larger solute diameters. As discussed earlier, the appearance of a second attractive interval within $z^*<\sigma$ arises because of the appearance of a maximum in the solvent-wall density profile, $\rho(z)$, for $z<\sigma$. Though one may expect solutes smaller than the solvent particles ($\sigma_s<\sigma$) to be strongly in-

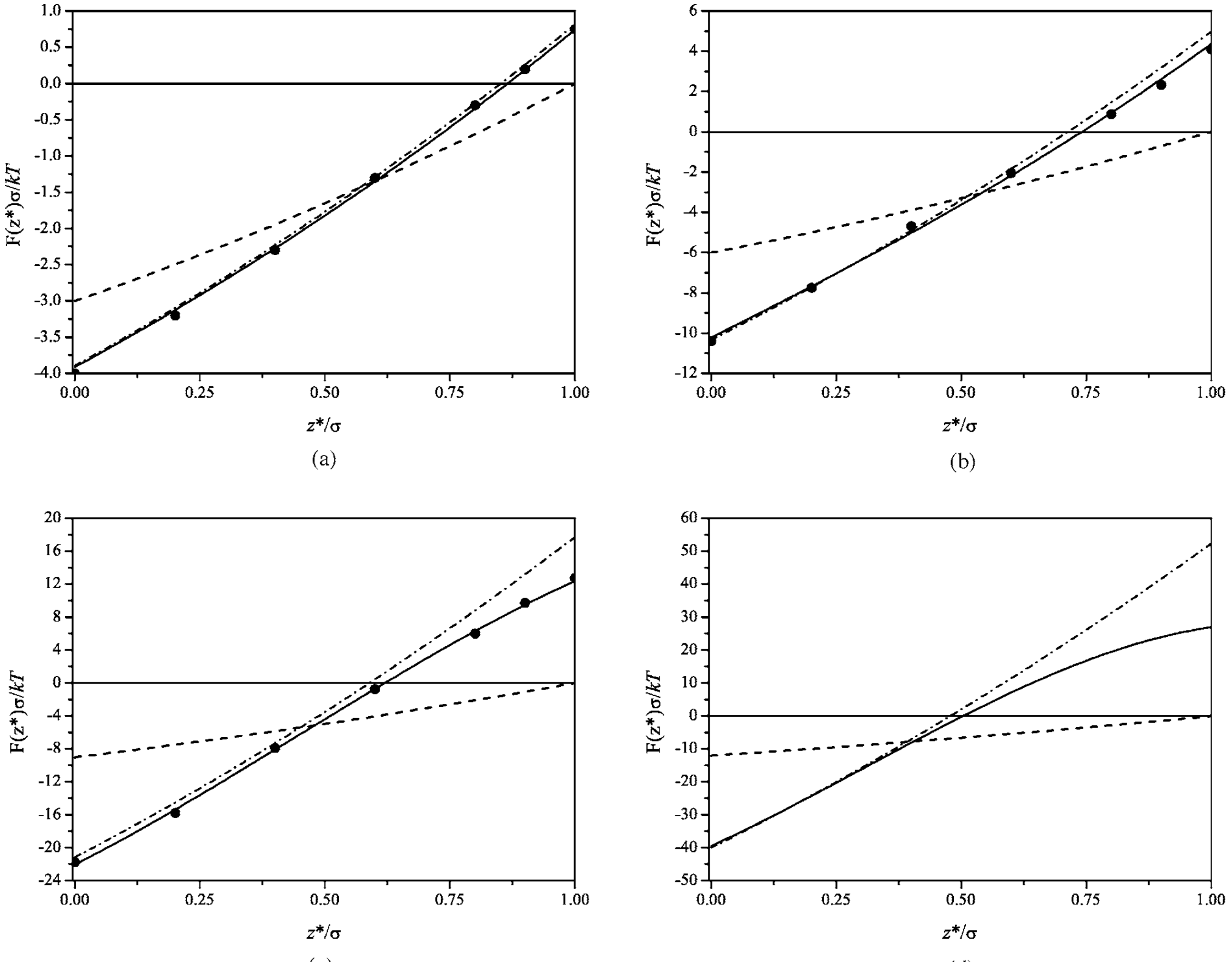

(a) (b) (c) (d)

FIG. 8. Entropic force, $F(z^*)$, between a hard-sphere solute of diameter $\sigma_s=5\sigma$ and a hard, flat wall at various packing fractions η. z^* specifies the distance between the wall and the surface of the solute. Solid lines represent the I-SPT results, the dashed-dotted lines are the predictions of Corti and Reiss [18], the dashed lines are the AO approximations [4], and the closed circles are the simulation results of Dickman *et al.* [24]. Clockwise from left, $\eta=0.1$, $\eta=0.2$, $\eta=0.4$, and $\eta=0.3$.

fluenced by $\rho(z)$, thereby exhibiting a second point at which $F=0$, such a conclusion may not have been fully anticipated for solute diameters exceeding σ, at least for diameters as large as 1.74σ.

In Fig. 10, the reversible work of cavity insertion for $\sigma_s=1.2\sigma$ ($\lambda=1.1\sigma$) and $\rho\sigma^3=0.914$ as obtained by I-SPT and MC simulation is presented. As expected, W exhibits both a maximum and a minimum for $z^*<\sigma$. Up to $z^*\approx 0.5\sigma$, the agreement between I-SPT and simulation is reasonably good. Large deviations between the two appear for $z^*>0.5\sigma$. Nevertheless, I-SPT still qualitatively captures the correct trends, yielding predictions for the two locations of $F=0$ (or $dW/dh=0$) that are close to the simulation results. The quantitative disagreement for $z^*\rightarrow\sigma$ is not unexpected for these intermediate solute diameters since the accuracy of our predictions near $z^*=\sigma$ depends upon the accuracy of f_{c3}. As shown in Appendix B, discrepancies between f_{c3} and simulation appear for solute diameters between $\sigma/2$ and σ (f_{c3} by definition matches simulation at σ) and slightly greater than σ. Although improvements at these diameters could be made by altering the chosen interpolation function for f_{c3} (as discussed in Appendix B), most depletion force profiles of interest are for larger solutes, where our I-SPT predictions already yield excellent agreement with simulation.

VII. FEATURES OF $\bar{F}(\lambda,h)$: THE ROLE OF GEOMETRY

While the overall behavior of the exact and interpolated plots of $\bar{F}(\lambda,h)$ was anticipated from geometric and physical arguments, certain aspects of $\bar{F}$ were, however, unexpected. In particular, $\bar{F}$ was always found to exhibit a maximum for $h<0$, before the solvent particles were able to access portions of the cavity surface at $\theta>\pi/2$ and counteract the force exerted by particles situated at $\theta<\pi/2$. How the local density of hard spheres around the cavity, or $\rho G(\lambda,\theta,h)$, varies with h provides an explanation for this trend, albeit an incomplete one. The geometry of the cavity configuration plays an important role that cannot be overlooked. Geometry is also important in fully understanding the location at which

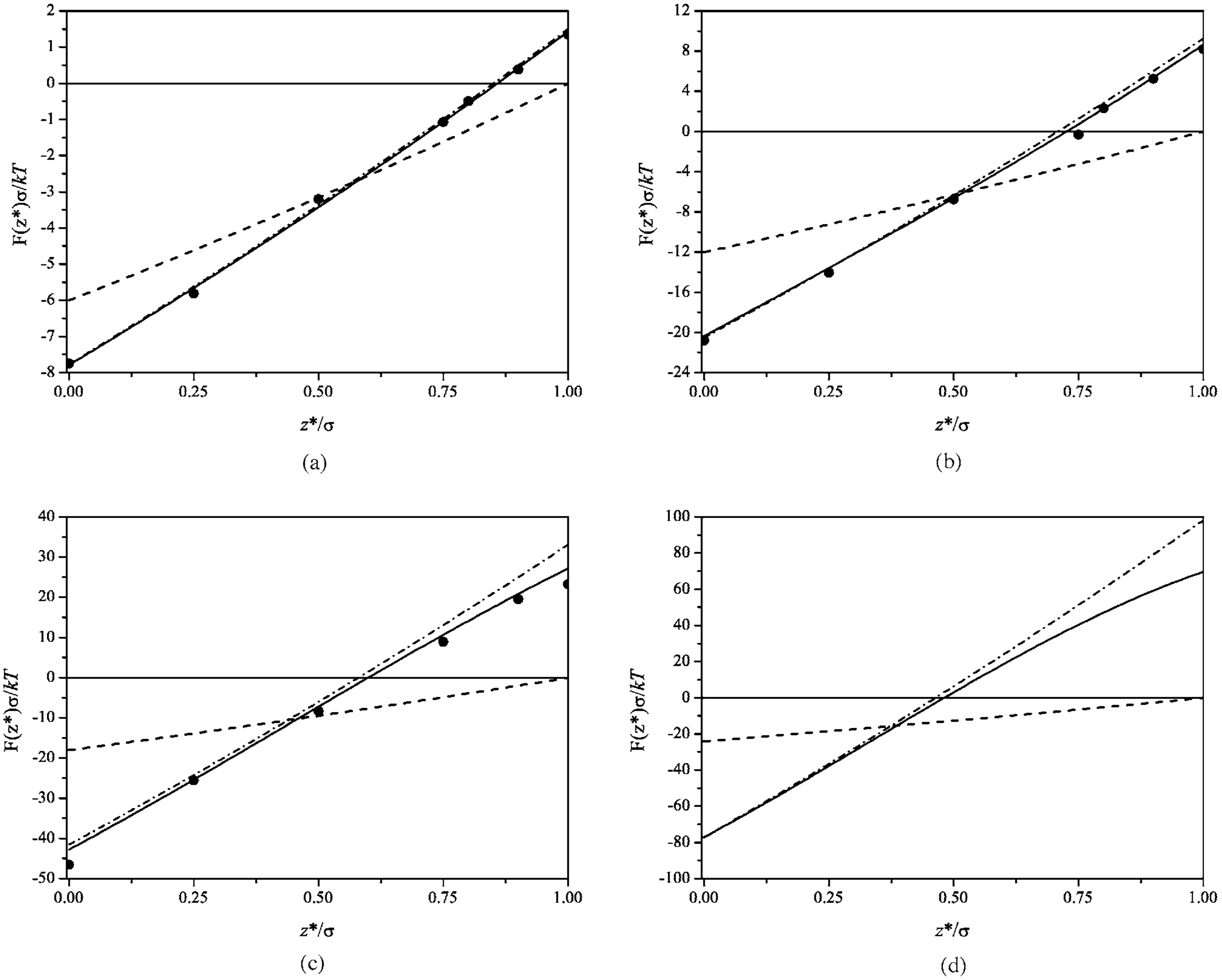

FIG. 9. Entropic force, $F(z^*)$, between a hard-sphere solute of diameter $\sigma_s=10\sigma$ and a hard, flat wall at various packing fractions η. Clockwise from left, $\eta=0.1$, $\eta=0.2$, $\eta=0.4$, and $\eta=0.3$. Data sources are identical to those in Fig. 8.

$\bar{F}$ vanishes for $h>0$. By providing more detailed analyses of these two aspects of $\bar{F}$, we highlight the interesting interplay between geometry and the anisotropic density profile that develops about the cavity, a not too widely appreciated effect that is important for developing a proper understanding of entropic forces in colloidal systems.

Although $G(\lambda,\theta,h)$ is not known in general, we consider its exact form for $\lambda\leqslant\sigma/2$, many features of which also appear at other values of λ and h [2]. As shown in Ref. [2], where an I-SPT-based integral equation for the local density about a cavity was derived, $G(\lambda,\theta,h)$ for $\lambda\leqslant\sigma/2$ is exactly given by

$$G(\lambda,\theta,h)=\frac{\rho(\lambda\cos\theta+h)}{\rho}\frac{1}{P_0(\lambda,h)}, \tag{27}$$

where $\rho(\lambda\cos\theta+h)$ is the local density of hard spheres at $z=\lambda\cos\theta+h$ (without a cavity present) and $P_0(\lambda,h)$ is the same as provided in Eq. (10). [Although Eq. (27) was derived in Ref. [2] only for $h\leqslant0$, the above relation is also valid for $h>0$ [42].] Since $P_0(\lambda,h)\leqslant1$, Eq. (27) requires that $\rho G(\lambda,\theta,h)\geqslant\rho(\lambda\cos\theta+h)$ for $\lambda\leqslant\sigma/2$, i.e., the local density at a particular point on the cavity surface is enhanced above that of the local solvent density (in the absence of the cavity) at the same location. For example, at $\theta_c=\cos^{-1}(-h/\lambda)$, corresponding to the intersection of the cavity surface and the $z=0$ plane, the local density exceeds $\rho(0)=p/kT$, the density of the hard-sphere solvent in contact with the $z=0$ plane (far from the cavity). The local density enhancement at θ_c increases with an increase in h (for fixed λ) since P_0 decreases with h. Upon geometric grounds, due to the even greater imbalance of collisions that result upon a particle approaching θ_c, one expects the density enhancement to be highest at θ_c and to increase as h increases (particularly for values of h at which θ_c exceeds $\pi/2$, when a cusplike region forms from the intersection of the $z=0$ plane and the cavity surface, see Fig. 1). In contrast, $\rho G(\lambda,\theta=0,h)$, although always exceeding $\rho(\lambda+h)$, may be smaller or larger than the bulk density ρ, since the density profile, $\rho(\lambda+h)$, may be smaller or larger than ρ, depending upon the values of λ and h.

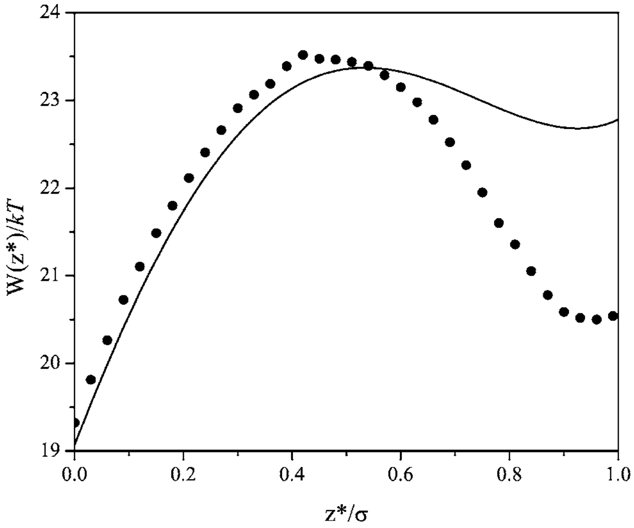

FIG. 10. Work of solute insertion, $W(z^*)$, for $\sigma_s/\sigma=1.2\sigma$ and $\rho\sigma^3=0.914$. The closed circles represent points generated by simulation and I-SPT calculations are plotted with the solid line.

A. Location of $\partial\bar{F}/\partial h=0$

Considering that a large density enhancement develops at $\theta_c \leq \pi/2$, which may yield a density several times greater than ρ, one might initially expect that the integral over $G(\lambda,\theta,h)$, and thus $\bar{F}$, to increase for $h<0$ as the upper integration bound, θ_c, increases with h. Consequently, the appearance of a maximum value, where $\partial\bar{F}/\partial h=0$, at $h<0$ is somewhat surprising. Although the expectation of a large density enhancement at θ_c is based on correct geometric arguments, the normal force exerted on the cavity that follows from the weighting of $G(\lambda,\theta,h)$ by $\sin\theta\cos\theta$ in Eq. (5) cannot be neglected. So while the density enhancement at θ_c continues to increase as θ_c approaches $\pi/2$, the normal component of the force exerted by the solvent continues to decrease. When the cavity is hemispherical ($h=0$), the solvent located at $\theta_c=\pi/2$, regardless of the density enhancement, offers no resistance to the further translation of the cavity in the z direction since $\cos\theta_c=0$. With $\sin\theta\cos\theta$ increasing from zero at $\theta=0$ to its maximum value at $\theta=\pi/4$ before decreasing back to zero again at $\theta=\pi$, the overall behavior of $\bar{F}$ arises from a competition between the density enhancement at θ_c, the potentially large density abatement that develops around $\theta=0$ and the value of $\sin\theta\cos\theta$.

Figure 11 displays $G(\lambda,\theta,h)\sin\theta\cos\theta$ as a function of θ for $\lambda=\sigma/2$, $\rho\sigma^3=0.5$ and several values of h, in which the area under each curve is simply equal to $\bar{F}(\lambda,h)$. $\bar{F}(\lambda,h)$ initially increases with an increase in h as the density enhancement around θ_c is still strongly weighted. Beyond $h=-0.135\sigma$ (not shown in figure), the total area under each curve begins to decrease because $\sin\theta\cos\theta$ is now able to reach the sufficiently small values needed to counteract the continuing increase in the local density at θ_c. In addition, the local density around $\theta=0$ has been drastically reduced and is weighted by a $\sin\theta\cos\theta$ term that is nearly zero. In other words, the collision of particle centers with the cavity surface becomes both concentrated at angles which contribute very little to the net force in the z direction and reduced at angles that have a larger normal contribution but smaller surface area, resulting in a reduction in the net force. The identical effect of the interplay between the local density variations and geometry is observed for smaller radii and, as suggested by our interpolation results and previous simulation studies [2], continues for larger radii. [Note that the emergence of negative $G(\lambda,\theta,h)\sin\theta\cos\theta$ values for $\theta>\pi/2$ does not by itself explain why the maximum in $\bar{F}$ resides at $h<0$. Although these negative values of the integrand serve to decrease $\bar{F}$, the positive values of $G(\lambda,\theta,h)\sin\theta\cos\theta$ for $\theta<\pi/2$ must either remain constant or decrease in order to see a net decrease in $\bar{F}$. If $G(\lambda,\theta,h)\sin\theta\cos\theta$ for $\theta<\pi/2$ began to increase, a maximum in $\bar{F}$ is not necessarily guaranteed to appear.]

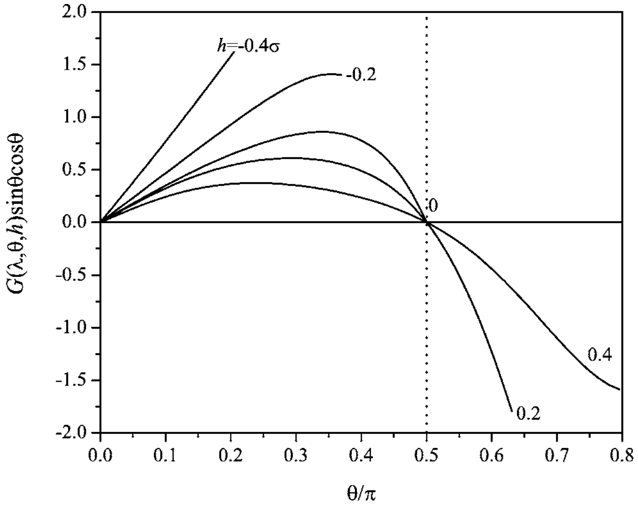

FIG. 11. The integrand of $\bar{F}(\lambda,h)$, or $G(\lambda,\theta,h)\sin\theta\cos\theta$, plotted as a function of θ for $\rho\sigma^3=0.5$ and $\lambda=\sigma/2$. Labels indicate the value of h for each line. $\bar{F}(\lambda,h)$ is the area under each curve. $\bar{F}(\lambda,h)$ initially increases with h before decreasing at an h between -0.2σ and 0. The actual maximum occurs at $h=-0.135\sigma$.

B. Location of $\bar{F}(\lambda,h)=0$

The eventual decrease of $\bar{F}$ toward negative values at $h>0$ indicates that the depletion force between the solute and the wall eventually becomes repulsive, a result not predicted by the original Asakura-Oosawa-Vrij model of depletion forces [4,5]. As suggested by Dickman *et al.* [24], a net repulsive force between a hard-sphere colloid and a hard wall develops when the local density at $\theta>\pi/2$ begins to outweigh the (attractively directed) collisions occurring at $\theta<\pi/2$. Although necessary, the density enhancement for $\theta>\pi/2$ is not a sufficient condition since geometry again plays an important role. The value of h for which $\bar{F}=0$, indicating a balance of repulsive and attractive forces, arises because collisions with the cavity surface finally become concentrated at angles exceeding $\pi/2$ with normal contributions large enough to counteract the lesser collisions occurring at $\theta<\pi/2$ with smaller surface area contributions.

Interestingly, the role of geometry is reversed here, as compared to its affect on the location of $\partial\bar{F}/\partial h=0$ at $h<0$. As seen in Fig. 11, when θ exceeds $\pi/2$ for $h>0$, $G\sin\theta\cos\theta$ becomes negative. As h increases, the local density at θ_c continues to increase while being weighted more heavily (in the negative direction) by $\sin\theta\cos\theta$ (note this weighting eventually decreases since $\sin\theta\cos\theta\to 0$ as $\theta\to\pi$). In contrast, the local density at $\theta<\pi/2$ decreases further, such that positive values of $G\sin\theta\cos\theta$ become less important. Eventually, the area under each curve, or $\bar{F}$, becomes negative. Therefore, the vanishing of $\bar{F}$ requires that the normal component of the local density behind the cavity be large enough to overcome the normal component in front of the cavity. If we identify the value of θ_c associated with $h=h_0(\lambda)$ (i.e., $\bar{F}=0$) as $\theta_c^0\equiv\cos^{-1}[-h_0(\lambda)/\lambda]$, we see that $\theta_c^0/\pi=2.8/4$ or $h=0.29\sigma$ for $\lambda=\sigma/2$ and $\rho\sigma^3=0.5$ (see Fig. 2) and $\theta_c^0/\pi\to 1$ or $h_0\to\lambda$ as $\lambda\to\infty$ at a fixed density. For macroscopic cavities, the local density along the cavity surface is constant, except for a small region near θ_c. Although a density enhancement is still present at θ_c, since that portion of the surface area of the cavity exposed to the density enhancement is becoming relatively smaller (as compared to the full cavity surface area) for $\lambda\to\infty$, an ever greater magnitude of $\cos\theta$ is needed to counteract the collisions for $\theta<\pi/2$, so that $\theta_c^0/\pi\to 1$ in the macroscopic limit. (Interestingly, the location of zero force is still found at a value of z^*, the distance between the wall and the surface of the solute, that is less than σ.) Finally, θ_c^0 is found to decrease with an increase in density, for a given λ, since the enhancement of the local density around θ_c^0 increases with bulk density such that, in general, a smaller $\cos\theta$ (or smaller h) is needed to balance the opposing collisions for $\theta<\pi/2$.

Additional complications arise for intermediate cavity sizes, where $\bar{F}=0$ at two values of $h>0$. The appearance of a second zero point suggests that the local density enhancement behind the cavity, despite its normal component becoming ever stronger, is no longer able to overcome the increasing strength of the collisions that occur in front of the cavity, is connected to the appearance of a local maximum in $\rho(z)$ for $z<\sigma$, which corresponds to an increase in the local density of solvent particles for $\theta<\pi/2$ at $\lambda\sim\sigma$. Although letting $h\to\lambda$ generates, as before, a sharp cusp and large density enhancement at θ_c, the corresponding small value of $\sin\theta_c$ now yields for intermediate cavity radii repulsive contributions that cannot overcome the density increase that develops for $\theta<\pi/2$ (while the cavity still intersects the $z=0$ plane). Clearly, a complete understanding of depletion interactions in hard colloid systems requires a detailed analysis of the complicated interplay between density variations and geometry.

VIII. CONCLUSIONS

A modified version of an inhomogeneous scaled particle theory allowing for the calculation of the reversible work of inserting a cavity that intersects a hard wall has been presented. In so doing, a new function, $\bar{F}(\lambda,h)$, was introduced, which is proportional to the net force experienced by the cavity in the direction normal to the wall. $\bar{F}$ is known exactly for certain cavity sizes and locations and is approximated beyond these limits via a set of interpolation polynomials. Predictions for the reversible work of cavity insertion are in very good agreement with simulation at all densities. Deviations from the simulation results do arise at high density for intermediate cavity sizes, in which the equivalent solutes have diameters close to that of the hard-sphere solvent, and are attributed to minor discrepancies that develop at these solute sizes for one of the matching conditions used within the chosen interpolation scheme.

Our new version of I-SPT can also be used to estimate the depletion force between a hard-sphere colloid and a hard, structureless wall. I-SPT predictions of the depletion force of large diameter colloids are in excellent agreement with simulation results, exhibiting regions of both attractive and repulsive force. Hence, I-SPT improves upon a previous bulk SPT-based method [18], which tended to overpredict the magnitude of the repulsive depletion force at high densities of the solvent.

Due to its reliance upon physical and geometric arguments, I-SPT yields important insights into the various features of $\bar{F}$. In particular, I-SPT clearly demonstrates that the transition between attractive and repulsive entropic forces is strongly influenced by the interplay between geometry and the variations of the local density around the cavity. Consequently, the entropic force for all solute sizes always vanishes for surface to wall separations that are less than the diameter of a hard-sphere solvent particle. At intermediate solute diameters, the effects of geometry and the variations in the local density serve to give rise to a second location at which the entropic force disappears, again within this same separation distance.

This current version of I-SPT is also extendable to the confined two-dimensional hard disk fluid. An exact expression for the two-dimensional version of $\bar{F}$ can be straightforwardly obtained, and is similar to the three-dimensional result presented here (the reduced dimensionality does, however, introduce some minor changes [42]). Beyond its exact limit, an interpolation of $\bar{F}$ is again needed, though a set of simple functions that adequately describes the two-dimensional version of $\bar{F}$ over its entire domain has yet to be identified.

Overall, I-SPT is a promising theoretical tool for analyzing the growth of cavities near a hard wall. Our current approach utilizes more exact information than any previous version of I-SPT, resulting in more accurate predictions as well as increased physical insight into the behavior of nonhomogeneous hard-particle fluids. While I-SPT has so far been specifically tailored to describe hard-particle fluids confined by hard, structureless walls, the methods presented here are readily extendable to nonplanar geometries, such as curved surfaces or surfaces with patterned microstructures. The equations may not be superficially simple, but SPT does offer advantages over other methods when analyzing these more complex surface geometries. Finally, when an expression for the line tension of cavities intersecting various surfaces is derived, I-SPT will provide the key information needed to calculate highly accurate estimates of this important thermodynamic property.

ACKNOWLEDGMENTS

This paper is based upon work supported by the National Science Foundation under Grant No. 0133780.

APPENDIX A: DIVERGENT BEHAVIOR OF $\partial^2\bar{F}/\partial h^2$ AND $\partial^2\bar{G}/\partial\lambda^2$ AT THEIR EXACT LIMITS

Using the coordinate system shown in Fig 1, consider that $P_0(\lambda,h)$, the probability of observing a cavity of radius of at least λ centered at $z=h$, is equivalent to the probability of finding a point on the $z=h$ plane that is a distance of at least λ from every hard-sphere center in the fluid. Hence, we may introduce spheres of radius λ centered about each hard sphere and consider their intersections with the $z=h$ plane. Now, the spheres of radius λ that intersect the $z=h$ plane project circles onto this plane, enclosing the area excluded to the center of a cavity of radius λ. Dividing the area not contained within these projected circles by the area of the $z=h$ plane yields $P_0(\lambda,h)$. Since the total area of the $z=h$ plane excluded to cavities is comprised of the area of overlapping circles, P_0 may be written in general as [3]

$$P_0(\lambda,h) = 1 - \sum_{m=1}^{\infty}(-1)^m F_m(\lambda,h), \tag{A1}$$

where $F_m(\lambda,h)$ is the fraction of the area on the $z=h$ plane enclosed within the mutual overlap of m circles projected on the plane by the spheres of radius λ. By analogy to Eq. (3.16) of Ref. [3], F_m is given by

$$F_m(\lambda,h) = \frac{1}{A_{\text{total}}\cdot m!}\int_{V_{\text{total}}}\cdots\int \rho^{[m]}(\mathbf{R}_1,\mathbf{R}_{2,}\ldots,\mathbf{R}_m)\Omega_m(\mathbf{R}_1,\mathbf{R}_{2,}\ldots,\mathbf{R}_m,\lambda,h)d\mathbf{R}_1\cdots d\mathbf{R}_m, \tag{A2}$$

in which $\Omega_m(\mathbf{R}_1,\mathbf{R}_{2,}\ldots,\mathbf{R}_m,\lambda,h)$ is the area on the $z=h$ plane enclosed within the mutual overlap of circles projected on the plane by m spheres of radius λ at positions $(\mathbf{R}_1,\mathbf{R}_{2,}\ldots,\mathbf{R}_m),\rho^{[m]}(\mathbf{R}_1,\mathbf{R}_{2,}\ldots,\mathbf{R}_m)d\mathbf{R}_1\cdots d\mathbf{R}_m$ is the probability of observing m hard spheres at the same positions and A_{total} is the total area of the $z=h$ plane. The ensemble average is obtained by integrating over V_{total}, the total volume occupied by the hard-sphere fluid.

Let us restrict our attention to the insertion of cavities centered at $h\leqslant 0$. Now, two spheres of radius λ concentric with two hard spheres will always have nonoverlapping projected circles on the $z=h$ plane when $\lambda^2\leqslant h^2+(\sigma/2)^2$. In this case, $F_m(\lambda,h)=0$ for $m\geqslant 2$, and we need only consider $F_1(\lambda,h)$, where

$$F_1(\lambda,h) = \frac{1}{A_{\text{total}}}\int_{V_{\text{total}}}\rho^{[1]}(\mathbf{R}_1)\Omega_1(\mathbf{R}_1,\lambda,h)d\mathbf{R}_1.$$

Since the fluid is symmetric in the directions parallel to the hard wall, Ω_1 and $\rho^{[1]}$ depend only on z, where $\rho^{[1]}(\mathbf{R}_1)=\rho(z)$ and $\Omega_1(\mathbf{R}_1,\lambda,h)=\pi[\lambda^2-(z-h)^2]$, the area projected onto the $z=h$ plane by the sphere of radius λ. With $\Omega_1=0$ for $z\geqslant h+\lambda$, and noting that $d\mathbf{R}_1=A_{\text{total}}dz$, F_1 reduces to

$$F_1(\lambda,h) = \pi\int_0^{h+\lambda}\rho(z)[\lambda^2-(z-h)^2]dz, \tag{A3}$$

so that

$$P_0(\lambda,h) = 1 - \pi\int_0^{h+\lambda}\rho(z)[\lambda^2-(z-h)^2]dz. \tag{A4}$$

The above relation is identical to Eq. (10), which was obtained via a different interpretation of P_0.

Two projected circles may overlap when $h^2+(\sigma/2)^2<\lambda^2\leqslant h^2+(\sigma/\sqrt{3})^2$, so that $F_2(\lambda,h)$ must be included in P_0 ($F_m=0$ for $m\geqslant 3$), where

$$F_2(\lambda,h) = \frac{1}{A_{\text{total}}\cdot 2!}\int\int_{V_{\text{total}}}\rho^{[2]}(\mathbf{R}_1,\mathbf{R}_2)\Omega_2(\mathbf{R}_1,\mathbf{R}_2,\lambda,h)d\mathbf{R}_1 d\mathbf{R}_2. \tag{A5}$$

Letting z_1 and z_2 be the z-directional distances of hard-spheres 1 and 2, respectively, and r the distance between their centers parallel to the hard wall, Eq. (A5) can be rewritten as

$$F_2(\lambda,h) = \pi\int_0^{h+\lambda}dz_1\int_0^{h+\lambda}dz_2\int_0^{r_{\max}}\rho^{[2]}(z_1,z_2,r)\Omega_2(z_1,z_2,r,\lambda,h)rdr, \tag{A6}$$

in which $r_{\max}=\sqrt{\lambda^2-(z_1-h)^2}+\sqrt{\lambda^2-(z_2-h)^2}$, the value of r for a given z_1 and z_2 at which Ω_2 vanishes. For our present purposes, the above expression can be simplified. We note that for $h^2+(\sigma/2)^2<\lambda^2\leqslant h^2+(\sigma/2)^2+\epsilon$, where ϵ is an exceedingly small quantity, the only configurations that generate a nonzero Ω_2 are those for which $z_1=z_2=0$. Thus, in the limit of $\epsilon\to 0$, F_2 reduces to

$$F_2(\lambda,h)=\pi\int_{\sigma}^{2\sqrt{\lambda^2-h^2}}\rho_{\mathrm{IP}}^{[2]}(0,r)\Omega_2(0,0,r,\lambda,h)r dr, \quad \text{(A7)}$$

where $\rho_{\mathrm{IP}}^{[2]}(z,r)$ is the two-dimensional (2D) probability density of finding two hard-sphere particles separated by a distance r given that both centers are located in the plane at z. Since $\rho_{\mathrm{IP}}^{[2]}(z,r)=0$ for $r<\sigma$, the lower limit of the integral has been set to σ. Equation (A7) is analogous to the $F_2(\lambda)$ term that appears in the P_0 expansion for the 2D hard-disk fluid [43], and so we expect $F_2(\lambda,h)$ to behave in a similar manner.

1. Discontinuous second derivative of $\bar{F}(\lambda,h)$

Following from Eq. (9), the ith derivative of $\bar{F}$ (with respect to h) is related to the $(i+1)$th and lower derivatives of P_0 or, from Eq. (A1), the $(i+1)$th and lower derivatives of each F_m. Thus, the behavior of the various derivatives of $\bar{F}(\lambda,h)$ evaluated at the limit of $h=-\sqrt{\lambda^2-(\sigma/2)^2}$, henceforth denoted $h_{\max}$, can be determined by examining each F_m and its derivatives at the same limit. Beginning with Eq. (A3), we see that F_1 and all of its derivatives with respect to h are well behaved, i.e., continuous at $h=h_{\max}$, provided $\rho(z)$ remains differentiable (which is an implicit assumption in our analysis). For larger h, specifically $h=h_{\max}+\epsilon$, where ϵ is an exceedingly small quantity, we must also consider the behavior of F_2 (higher-order terms are still zero at this h value). For $\epsilon\to 0$, we may examine the two-dimensional form of F_2 provided in Eq. (A7). For the case of $z_1=z_2=0$, the area of intersection of the two circles projected on the $z=h$ plane is given by

$$\Omega_2(0,0,r,\lambda,h)=\left[2\cos^{-1}\left(\frac{r}{2\sqrt{\lambda^2-h^2}}\right)-\frac{r\sqrt{\lambda^2-h^2-\left(\frac{r}{2}\right)^2}}{\lambda^2-h^2}\right](\lambda^2-h^2). \quad \text{(A8)}$$

Substituting the above into Eq. (A7), one can show that

$$F_2(\lambda,h_{\max})=0, \qquad \left.\frac{\partial F_2}{\partial h}\right|_{h=h_{\max}}=0, \quad \text{(A9)}$$

which, along with the continuity of F_1 and its derivatives, imply that $\bar{F}$ is continuous at $h=h_{\max}$.

If F_2 is differentiated twice with respect to h, the term which remains upon letting $\epsilon\to 0$ is

$$\frac{\partial^2 F_2}{\partial h^2}=\pi\int_{\sigma}^{2\sqrt{\lambda^2-h^2}}\rho_{\mathrm{IP}}^{[2]}(0,r)\frac{\partial^2\Omega_2(0,0,r,\lambda,h)}{\partial h^2}r dr. \quad \text{(A10)}$$

Now, $\partial^2\Omega_2/\partial h^2\to\infty$ at $r=2\sqrt{\lambda^2-h_{\max}^2}=\sigma$, so it is not readily apparent if the above integral vanishes. To proceed further, we instead return to Eq. (A7) and replace $\rho_{\mathrm{IP}}^{[2]}(0,r)$ with a series expansion whose first term is given by $\rho_{\mathrm{IP}}^{[2]}(0,\sigma)$, the contact value of this 2D pair correlation function. Integration then yields

$$F_2(\lambda,h)=\frac{\pi\rho_{\mathrm{IP}}^{[2]}(0,\sigma)}{8}\left[\frac{\sigma}{4}\sqrt{\lambda^2-h^2-\frac{\sigma^2}{4}}(2\lambda^2-2h^2+\sigma^2)+(\lambda^2-h^2)(\lambda^2-h^2-\sigma^2)\cos^{-1}\left(\frac{\sigma}{2\sqrt{\lambda^2-h^2}}\right)\right]+\cdots, \quad \text{(A11)}$$

where, for the present analysis, we need only consider the lowest order terms. The first derivative of the above, as previously mentioned, vanishes at $h=h_{\max}$. Performing two additional derivatives reveals that

$$\left.\frac{\partial^2 F_2}{\partial h^2}\right|_{h=h_{\max}}=0, \qquad \left.\frac{\partial^3 F_2}{\partial h^3}\right|_{h\to h_{\max}}\to\infty, \quad \text{(A12)}$$

implying that

$$\left.\frac{\partial^2\bar{F}}{\partial h^2}\right|_{h\to h_{\max}}\to -\infty. \quad \text{(A13)}$$

While $\partial\bar{F}/\partial h$ is continuous at $h_{\max}$, $\partial^2\bar{F}/\partial h^2$ diverges to $-\infty$ as $h_{\max}$ is approached from above (from below, $\partial^2\bar{F}/\partial h^2$ approaches a finite value; all higher-order derivatives of $\bar{F}$ behave in a similar manner). Although the divergence of $\partial^2\bar{F}/\partial h^2$ could be incorporated into an interpolation scheme, this information does not appear to be needed to accurately compute W, even at high densities. Given that $h_{\max}$, particularly for large λ, is close to the lower limit of $h=-\lambda$, the influence of the discontinuous and divergent curvature of $\bar{F}$ should be relatively short ranged, considering the importance of the many other conditions on $\bar{F}$ that are invoked over $0\leqslant h\leqslant\lambda$.

2. Discontinuous second derivative of $\bar{G}(\lambda,h)$

We now examine the derivatives of $\bar{G}(\lambda,h)$ at the limit of $\lambda=\sqrt{h^2+(\sigma/2)^2}$, denoted by $\lambda_{\max}$. As shown in Ref. [1], $\bar{G}$ is related to P_0 according to

$$\rho\bar{G}(\lambda,h)=\frac{-1}{2\pi(\lambda^2+\lambda h)}\frac{\partial\ln P_0}{\partial\lambda}, \quad \text{(A14)}$$

so that the ith derivative of $\bar{G}$ with respect to $(i+1)$th and lower derivatives of each F_m appearing in Eq. (A1). Similar to the above analysis of $\bar{F}$, all derivatives of F_1 with respect to λ are well behaved at $\lambda_{\max}$ [again provided that $\rho(z)$ is differentiable]. Next, we consider the various derivatives of F_2 with respect to λ. For $\lambda=\lambda_{\max}+\epsilon$, we again begin with Eq. (A11), which upon differentiation and letting $\epsilon\to 0$ yields

$$F_2(\lambda_{\max},h)=0, \qquad \left.\frac{\partial F_2}{\partial\lambda}\right|_{\lambda=\lambda_{\max}}=0,$$

$$\left.\frac{\partial^2 F_2}{\partial\lambda^2}\right|_{\lambda=\lambda_{\max}}=0, \qquad \left.\frac{\partial^3 F_2}{\partial\lambda^3}\right|_{\lambda\to\lambda_{\max}}\to\infty. \tag{A15}$$

Therefore, $\bar{G}$ and $\partial\bar{G}/\partial\lambda$ are continuous at $\lambda_{\max}$, while

$$\left.\frac{\partial^2\bar{G}}{\partial\lambda^2}\right|_{\lambda\to\lambda_{\max}}\to-\infty. \tag{A16}$$

Since $\partial^2\bar{G}/\partial\lambda^2$ is discontinuous and diverges as $\lambda_{\max}$ is approached from above (from below, $\partial^2\bar{G}/\partial\lambda^2$ approaches a finite value), all higher derivatives at $\lambda_{\max}$ will diverge in a similar manner.

3. Improved interpolation of $\bar{G}(\lambda)$

Last, we introduce an updated version of our approximate form of $\bar{G}$ for $h=0$ and $\lambda>\sigma/2$, which now includes the divergence of $\partial^2\bar{G}/\partial\lambda^2$ as $\lambda\to\sigma/2$ [$\bar{G}$ is still computed exactly for $\lambda\leqslant\sigma/2$ via Eq. (20) of Ref. [1]]. Owing to the differences between the simulation and I-SPT predictions of W for a hemispherical cavity at high density [1], along with the importance of an accurate $\bar{G}$ through its use in providing a condition on $\bar{F}$, we were motivated to incorporate additional information on $\bar{G}$ to improve our calculation of W for $h=0$. Unlike the other exact conditions on $\bar{G}$ [1], one may not simply choose $\partial^2\bar{G}/\partial\lambda^2=-\infty$ at a particular λ; this divergence must be explicitly included in the functional form of the chosen interpolation scheme [44].

To incorporate properly the known divergence, we begin with Eq. (A7), where we approximate the unknown function $\rho_{\mathrm{IP}}^{[2]}(0,r)$, by

$$\rho_{\mathrm{IP}}^{[2]}(0,r)=\rho_{\mathrm{IP}}^{[2]}(0,\sigma)\exp[-a(r-\sigma)], \qquad r\geqslant\sigma, \tag{A17}$$

in which a is a positive decay constant. With the above, $F_2(\lambda)$ becomes

$$F_2(\lambda)=\psi\int_{\sigma}^{2\lambda}\exp[-a(r-\sigma)]\Omega_2(0,0,r,\lambda)r\,dr, \tag{A18}$$

where ψ is another density-dependent adjustable parameter [$\psi=\pi\rho_{\mathrm{IP}}^{[2]}(0,\sigma)>0$, where $\rho_{\mathrm{IP}}^{[2]}(0,\sigma)$ is not known in general]. Using Eq. (A1), we now represent P_0 for $\sigma/2<\lambda\leqslant\lambda_m$ with

$$P_0(\lambda)=1-\pi\int_0^{\lambda}\rho(z)(\lambda^2-z^2)dz+\psi\int_{\sigma}^{2\lambda}\exp[-a(r-\sigma)]\Omega_2(0,0,r,\lambda)r\,dr,$$
$$\frac{\sigma}{2}<\lambda\leqslant\lambda_m. \tag{A19}$$

For $\lambda>\lambda_m$, $\bar{G}$ is again interpolated via the following Laurent series expansion

$$\bar{G}(\lambda)=\beta_0(\rho)+\frac{\beta_1(\rho)}{\lambda}+\frac{\beta_2(\rho)}{\lambda^2}+\frac{\beta_4(\rho)}{\lambda^4}, \qquad \lambda>\lambda_m. \tag{A20}$$

Given the above expression for P_0, $\partial^2\bar{G}/\partial\lambda^2$ is ensured to diverge towards $-\infty$ in the required manner as $\lambda\to\sigma/2$ (as well as ensuring that $\bar{G}$ and $\partial\bar{G}/\partial\lambda$ are continuous at $\lambda=\sigma/2$). As before, matching conditions are needed to identify the various interpolation parameters, in this case a, ψ, and the four $\beta_i(\rho)$. Two conditions are imposed by thermodynamics: $\beta_0(\rho)=p/\rho kT$ and $\beta_1(\rho)=\gamma_\infty/\rho kT$. (The condition on β_1 was not originally invoked in Ref. [1]. Just as the density in contact with the surface of the hemispherical cavity should approach p/kT in the planar limit, $\lambda\to\infty$, so should the leader order area term in the resulting macroscopic work expression be related to the planar boundary tension γ_∞. In the bulk SPT interpolation function, this area term is related to $2\gamma_\infty$, which for a full spherical cavity is simply 2 times the hemispherical result.) The other four matching conditions are chosen to be the continuity of $\bar{G}$ and its first two derivatives at λ_m and the condition on $W(\sigma)$ as provided by Eq. (23) of Ref. [1]. λ_m is still to be determined, though it must fall between $\sigma/2$ and $\sigma/\sqrt{3}$ (so that P_0 is only expressed by F_1 and F_2) and yield positive values of a and ψ. The interpolation parameters were obtained by preselecting λ_m, and then solving numerically via an iterative Newton-Raphson algorithm with a residual tolerance of 10^{-6}. When a and ψ are both positive, a valid solution was found. In examining various valid solutions, we found that the resulting values of W were not greatly sensitive to λ_m. At low densities only (for example, $\rho\sigma^3=0.3$), the new approximation did not always yield a solution (solutions were always found for $\rho\sigma^3\geqslant0.6$). In this case, the old interpolation scheme was used, which was already shown to be extremely accurate [1].

Table I displays $W(\lambda)$ for $\rho\sigma^3=0.6$ and 0.914 as calculated by simulation, the previous I-SPT interpolation method, and the improved approximation. For $\rho\sigma^3=0.6$, the improved interpolation does not greatly modify W for any λ. At $\rho\sigma^3=0.914$, where the older I-SPT interpolation significantly underpredicted W, we find that the new interpolation approximation of $\bar{G}$ significantly improves the I-SPT predictions of W, reducing the error to 1.21% at $\lambda=3\sigma$ (most likely within the error bars of the simulation results).

TABLE I. Work of hemispherical cavity insertion, $W(\lambda)/kT$, computed by MC simulation (marked Sim.), the original I-SPT [1], and the improved I-SPT approximation (marked Imp. I-SPT). The row above each data set identifies the reduced density, $\rho\sigma^3$, far from the wall and λ_m used for the I-SPT approximation. This row also displays the fitting parameters ψ and a. The columns marked Error list the error of the adjacent I-SPT calculation relative to MC simulation.

	$\rho\sigma^3=0.6$	$\lambda_m=0.5075\sigma$		$\psi=0.28/\sigma^4$	$a=6.65/\sigma$
λ/σ	Sim [1]	I-SPT [1]	% Error	Imp. I-SPT	% Error
0.75	1.47	1.49	1.40%	1.49	1.38%
1.0	3.81	3.87	1.61%	3.87	1.61%
1.5	14.50	14.50	0.06%	14.51	0.08%
2.0	36.29	36.34	0.13%	36.35	0.15%
3.0	129.48	129.77	0.22%	129.80	0.25%
	$\rho\sigma^3=0.914$	$\lambda_m=0.515\sigma$		$\psi=4.15/\sigma^4$	$a=16.77/\sigma$
λ/σ	Sim [1]	I-SPT [1]	% Error	Imp. I-SPT	% Error
0.75	4.32	4.47	3.63%	4.29	−0.54%
1.0	12.40	12.37	−0.25%	12.37	−0.24%
1.5	50.95	47.92	−5.95%	50.87	−0.16%
2.0	131.65	122.73	−6.77%	132.70	0.80%
3.0	485.30	454.22	−6.40%	491.19	1.21%

APPENDIX B: DERIVATION OF THERMODYNAMIC CONDITIONS ON $\bar{F}(\lambda,h)$

In this appendix, we derive a number of conditions on the I-SPT function $\bar{F}(\lambda,h)$ that are employed in the proposed interpolation scheme for $\bar{F}$. These conditions are generated by invoking the surface thermodynamics of macroscopic cavities and are valid only for macroscopic cavities that intersect the $z=0$ plane.

1. A general thermodynamic condition on $\bar{F}(\lambda,h)$

We begin by introducing the following macroscopic expression for the differential work of growing a cavity that intersects the $z=0$ plane,

$$dW = p\,dV + d(\gamma_r A) - \gamma_\infty dA_{\text{wall}} + d(\tau L). \tag{B1}$$

As shown above, the reversible work of cavity growth may be divided into four separate terms: the pressure-volume work (pdV), the work required to create the curved surface of the cavity $[d(\gamma_r A)]$, the work required to eliminate a portion of the wall-fluid interface ($\gamma_\infty dA_{\text{wall}}$), and the work required to create the linear interface $[d(\tau L)]$ where the fluid, wall, and cavity converge. $\gamma_r<0$ is the surface (or boundary) tension of the cavity (placed in the bulk fluid) based on a dividing surface chosen coincident with the cavity radius λ and A is that portion of the surface area of the cavity residing to the right of the $z=0$ plane. $\gamma_\infty<0$ is the surface tension in the planar limit and A_{wall} is the area of the $z=0$ plane that is overlapped by the cavity. Finally, τ is the line tension [45,46] of the linear interface of length L. For the cavity geometry shown in Fig. 1, Eq. (B1) implies that

$$\frac{dW}{dh} = 2\pi\rho kT\lambda^2\bar{F}(\lambda,h) = \pi p(\lambda^2-h^2) + 2\pi\lambda\gamma_r + 2\pi h\gamma_\infty + \frac{\partial(\tau L)}{\partial h}, \tag{B2}$$

where dW/dh is related to $\bar{F}$ by Eqs. (4) and (6). [In Eq. (B2) we have allowed τL to vary with h, although this dependence is unknown at present. How τL depends upon h will become inconsequential, however, since with the plausible assumption that τL and its derivative are finite and represent lower order contributions than the surface and volume terms, $\partial(\tau L)/\partial h$ will become insignificant, relatively speaking, as $\lambda\to\infty$.] Next, let $h=\lambda-\delta$, where δ is a positive value less than λ but on the order of σ, which upon substitution into Eq. (B2) yields

$$\lambda\bar{F}(\lambda,\lambda-\delta) = \frac{p\delta}{\rho kT} - \frac{p\delta^2}{2\rho kT\lambda} + \frac{\gamma_r}{\rho kT} + \frac{\gamma_\infty}{\rho kT} - \frac{\gamma_\infty\delta}{\rho kT\lambda} + \frac{1}{2\pi\rho kT\lambda}\frac{\partial(\tau L)}{\partial h}. \tag{B3}$$

Taking the limit as $\lambda\to\infty$, we find that

$$\lim_{\lambda\to\infty}[\lambda\bar{F}(\lambda,\lambda-\delta)] = \frac{p\delta+2\gamma_\infty}{\rho kT}, \tag{B4}$$

where $\gamma_r\to\gamma_\infty$. Equation (B4) represents a generalized condition on $\bar{F}$ in the limit of $\lambda\to\infty$, in which there is a free parameter $\delta<\lambda$, and is identical to the well-known Derjaguin limit for the force between a colloid and a flat wall [47]. The following sections make use of this generalized condition on $\bar{F}$ to develop a number of more specific conditions.

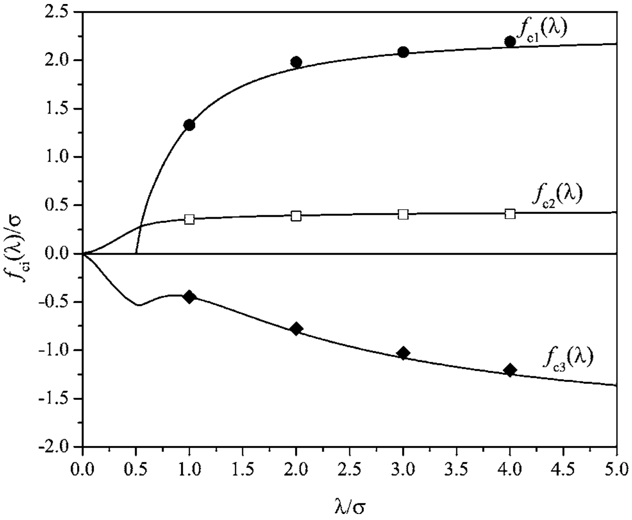

FIG. 12. The three interpolation functions, f_{c1}, f_{c2}, and f_{c3} plotted as a function of cavity radius λ for $\rho\sigma^3=0.6$. Solid lines are I-SPT predictions, while the filled circles, open squares, and filled diamonds represent MC simulation results for f_{c1}, f_{c2}, and f_{c3}, respectively.

2. Condition for $h=\lambda-\sigma$

The first thermodynamic condition on $\bar{F}$ is developed by selecting $\delta=\sigma$, so that Eq. (B4) becomes

$$\lim_{\lambda\to\infty}[\lambda\bar{F}(\lambda,\lambda-\sigma)]=\frac{p\sigma+2\gamma_\infty}{\rho kT},\tag{B5}$$

which constrains $\bar{F}$ at $h=\lambda-\sigma$ in the macroscopic limit and is an *exact* condition on the quantity $\lambda\bar{F}(\lambda,\lambda-\sigma)$. Since $\bar{F}$ is known exactly for $-\lambda\leqslant h\leqslant-\sqrt{\lambda^2-(\sigma/2)^2}$, $f_{c1}(\lambda)=\lambda\bar{F}(\lambda,\lambda-\sigma)$ is also known *exactly* for $\lambda\leqslant5\sigma/8$. Following from arguments presented in Appendix A regarding $\bar{F}$ and $\partial\bar{F}/\partial\lambda$, f_{c1} and $df_{c1}/d\lambda$ are also continuous at $\lambda=5\sigma/8$. [This exact limit is identified by inserting $h=\lambda-\sigma$ into the inequality $h\leqslant-\sqrt{\lambda^2-(\sigma/2)^2}$, which defines the upper bound of the exact domain of h. After replacing h with $\lambda-\sigma$ and some manipulation, one finds that $h=\lambda-\sigma$ falls in the exact domain of h for $\lambda\leqslant5\sigma/8$.]

3. Condition for $\bar{F}[\lambda,h_0(\lambda)]=0$

A second condition on $\bar{F}$ is identified by defining $h_0(\lambda)$ such that $\bar{F}[\lambda,h_0(\lambda)]=0$. Introducing $\delta=\lambda-h_0(\lambda)$ into Eq. (B4) yields upon setting $\bar{F}(\lambda,\lambda-\delta)=0$,

$$0=\left.\frac{p[\lambda-h_0(\lambda)]+2\gamma_\infty}{\rho kT}\right|_{\lambda\to\infty},\tag{B6}$$

which requires that

$$\lim_{\lambda\to\infty}[\lambda-h_0(\lambda)]=\frac{-2\gamma_\infty}{p}.\tag{B7}$$

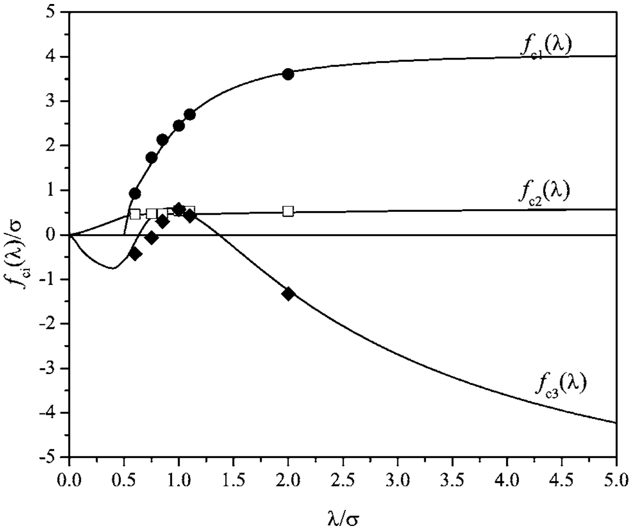

FIG. 13. The three interpolation functions, f_{c1}, f_{c2}, and f_{c3} plotted as a function of cavity radius λ for $\rho\sigma^3=0.914$. Data sources and identification are identical to those in Fig. 12. $f_{c3}>0$ for $0.64\sigma<\lambda<1.37\sigma$, which is in contrast to its behavior at lower densities ($\rho\sigma^3\lesssim0.8$) where $f_{c3}<0$ for all λ.

[This limiting value can also be derived directly from Eq. (B3).] As before, exact knowledge of $\bar{F}$ enables us to determine h_0 for $\lambda\leqslant\sigma/2$. To obtain $h_0(\sigma/2)$, we set $\bar{F}[\sigma/2,h_0(\sigma/2)]=0$, which upon using Eq. (11) requires that

$$\int_0^{h_0(\sigma/2)+\sigma/2}\rho(z)[z-h_0(\sigma/2)]dz=0.\tag{B8}$$

Solution for $h_0(\sigma/2)$ is accomplished by trial and error. Furthermore, exact knowledge of $\bar{F}$ also provides information regarding the derivative of h_0 at $\lambda=\sigma/2$. Taking a derivative of $\bar{F}[\lambda,h_0(\lambda)]=0$, as based upon Eq. (11), with respect to λ and setting $\lambda=\sigma/2$, yields upon further arrangement

$$\left.\frac{\partial h_0(\lambda)}{\partial\lambda}\right|_{\lambda=\sigma/2}=\frac{\sigma\rho\left[\frac{\sigma}{2}+h_0\left(\frac{\sigma}{2}\right)\right]}{2\int_0^{h_0(\sigma/2)+\sigma/2}\rho(z)dz-\sigma\rho\left[\frac{\sigma}{2}+h_0\left(\frac{\sigma}{2}\right)\right]}.\tag{B9}$$

4. Condition for $h=\lambda$

The final condition is obtained for $h=\lambda$, i.e., $\delta=0$. With this choice of δ, Eq. (B4) becomes

$$\lim_{\lambda\to\infty}[\lambda\bar{F}(\lambda,\lambda)]=\frac{2\gamma_\infty}{\rho kT}.\tag{B10}$$

Again through knowledge of $\bar{F}$ up to $\lambda=\sigma/2$, $\bar{F}(\lambda,\lambda)$ is known exactly up to $\lambda=\sigma/2$ (rather than $5\sigma/8$).

5. Validation of thermodynamic conditions

To test the validity of the interpolation functions, f_{ci}, proposed in Sec. III B 2, which incorporate both the macroscopic and small cavity conditions derived above (as well as other information for $\lambda=\sigma$), we compare the predictions of Eq. (24) with the results of molecular simulation. As discussed previously, all thermodynamic properties of the hard-sphere fluid, such as p and γ_∞, were computed using the Carnahan-Starling equation of state (CS-EOS [28]), where we utilize an adaptation of SPT to the CS-EOS [22,29] to compute γ_∞ (which yields results in good agreement with both a semiempirical expression [41] and other simulation predictions [39,40]). Polynomial fits of the simulation-generated density profiles were used to compute the needed derivatives of $\rho(z)$ for the small cavity conditions on f_{ci}. See Sec. III B 2 for a detailed discussion of all the information that was used to solve for the various coefficients utilized in Eq. (24).

Figure 12 displays all three interpolation functions, f_{c1}, f_{c2}, and f_{c3}, plotted versus λ for $\rho\sigma^3=0.6$. As expected, $f_{c1}\geqslant 0$, $f_{c2}\geqslant 0$, and $f_{c3}\leqslant 0$ at this moderate fluid density. For $\lambda<\sigma/2$, $f_{c1}=0$, which is expected since $\bar{F}(\lambda,h)=0$ for $h\leqslant\lambda$. All three conditions begin at zero, and then increase or decrease to their asymptotic limit (the three macroscopic limits derived above). At this density, f_{c3} exhibits a small change in shape for λ slightly larger than $\sigma/2$, a result of an abrupt change in curvature. The change in curvature is not present at a lower density, and is an anticipation of the change that occurs at larger densities where $f_{c3}>0$ around $\lambda\approx\sigma$. The other functions do not exhibit complex behavior; f_{c1} and f_{c2} are always positive, and show monotonic behavior, at all densities. Our I-SPT predictions match the simulation results quite well.

To illustrate the complicated behavior exhibited by f_{c3} at high densities, Figure 13 shows the same interpolation functions for $\rho\sigma^3=0.914$. f_{c1} and f_{c2} are qualitatively identical to the results seen in Fig. 12. In contrast, f_{c3} does not simply decay to its infinite limit. While the initial slope of f_{c3} is negative, a local minimum develops before $\lambda=\sigma/2$ in which $f_{c3}(\lambda)$ becomes positive for $0.64\sigma<\lambda<1.37\sigma$ [and as such $\bar{F}(\lambda,\lambda)$ is positive instead of its usual negative value in this range]. Beyond these radii, f_{c3} remains negative and decreases asymptotically to its final value, though much slower than that in Fig. 12. The interpolation deviates somewhat from the simulation results between $\lambda=\sigma/2$ and σ, but appears to be accurate for $\lambda>\sigma$ (note that f_{c3} is known exactly for $\lambda\leqslant\sigma/2$ as well as $\lambda=\sigma$). This discrepancy for $\sigma/2<\lambda<\sigma$ may be related to a discontinuity in the second derivative of $f_{c3}(\lambda)$ at $\lambda=\sigma/2$, which apparently exhibits divergent behavior at its exact limit, much like $\partial^2\bar{F}/\partial\lambda^2$ and $\partial^2\bar{G}/\partial\lambda^2$ (see Appendix A). The exact nature of this discontinuity is, however, unclear at present, but once known could be incorporated into the interpolation method as was done for $\bar{G}$ in Appendix A.

[1] D. W. Siderius and D. S. Corti, Phys. Rev. E **71**, 036141 (2005).
[2] D. W. Siderius and D. S. Corti, Phys. Rev. E **71**, 036142 (2005).
[3] H. Reiss, H. L. Frisch, and J. L. Lebowitz, J. Chem. Phys. **31**, 369 (1959).
[4] S. Asakura and F. Oosawa, J. Chem. Phys. **22**, 1255 (1954).
[5] A. Vrij, Pure Appl. Chem. **48**, 471 (1976).
[6] A. D. Dinsmore, A. G. Yodh, and D. J. Pine, Nature (London) **383**, 239 (1996).
[7] J. Y. Walz and A. Sharma, J. Colloid Interface Sci. **168**, 485 (1994).
[8] B. Götzelmann, R. Evans, and S. Dietrich, Phys. Rev. E **57**, 6785 (1998).
[9] W. R. Smith and R. J. Speedy, J. Chem. Phys. **86**, 5783 (1987).
[10] S. Labík, W. R. Smith, and R. J. Speedy, J. Chem. Phys. **88**, 1944 (1988).
[11] S. Labík and W. R. Smith, J. Chem. Phys. **88**, 3893 (1988).
[12] H. Reiss, J. Phys. Chem. **96**, 4736 (1992).
[13] D. Frenkel, J. Phys.: Condens. Matter **6**, A71 (1994).
[14] X. Chu, A. D. Nikolov, and D. T. Wasan, Chem. Eng. Commun. **150**, 123 (1996).
[15] T. Biben, P. Bladon, and D. Frenkel, J. Phys.: Condens. Matter **8**, 10799 (1996).
[16] H. H. von Grunberg and R. Klein, J. Chem. Phys. **110**, 5421 (1999).
[17] K. H. Lin, J. C. Crocker, V. Prasad, A. Schofield, D. A. Weitz, T. C. Lubensky, and A. G. Yodh, Phys. Rev. Lett. **85**, 1770 (2000).
[18] D. S. Corti and H. Reiss, Mol. Phys. **95**, 269 (1998).
[19] M. J. Mandell and H. Reiss, J. Stat. Phys. **13**, 107 (1975).
[20] M. D. Heying and D. S. Corti, J. Phys. Chem. B **108**, 19756 (2004).
[21] H. Reiss, "Scaled particle theory of hard sphere fluids to 1976," *Statistical Mechanics and Statistical Methods in Theory and Application: A Tribute to Elliott W. Montroll* (Plenum, London, 1977), p. 99.
[22] D. W. Siderius and D. S. Corti, Ind. Eng. Chem. Res. **45**, 5489 (2006).
[23] M. J. Mandell and H. Reiss, J. Stat. Phys. **13**, 113 (1975).
[24] R. Dickman, P. Attard, and V. Simonian, J. Chem. Phys. **107**, 205 (1997).
[25] R. C. Tolman, *Principles of Statistical Mechanics* (Oxford University Press, London, 1938).
[26] B. Widom, J. Stat. Phys. **19**, 563 (1978).
[27] B. Widom, J. Phys. Chem. **86**, 869 (1982).
[28] N. F. Carnahan and K. E. Starling, J. Chem. Phys. **51**, 635 (1969).
[29] D. W. Siderius and D. S. Corti (unpublished).
[30] B. J. Adler and T. E. Wainwright, J. Chem. Phys. **27**, 1208 (1957).
[31] W. W. Wood and J. D. Jacobson, J. Chem. Phys. **27**, 1207 (1957).
[32] W. G. Hoover and F. H. Ree, J. Chem. Phys. **48**, 3609 (1968).
[33] R. Bragado and G. Navascues, J. Chem. Phys. **68**, 2971 (1979).
[34] R. Bragado and G. Navascues, Phys. Rev. A **29**, 2134 (1984).

[35] J. E. Finn and P. A. Monson, Mol. Phys. **65**, 1345 (1988).
[36] J. E. Finn and P. A. Monson, Langmuir **5**, 639 (1989).
[37] D. Frenkel and B. Smit, *Understanding Molecular Simulation* (Academic, San Diego, 1996).
[38] S. Punnathanam and D. S. Corti, Ind. Eng. Chem. Res. **41**, 1113 (2002).
[39] J. R. Henderson and F. van Swol, Mol. Phys. **51**, 991 (1984).
[40] P. Attard and G. A. Moule, Mol. Phys. **78**, 943 (1993).
[41] D. Henderson and M. Plischke, Proc. R. Soc. London, Ser. A **410**, 409 (1987).
[42] D. W. Siderius, Master's thesis, Purdue University, West Lafayette, Indiana, 2004.
[43] E. Helfand, H. L. Frisch, and J. L. Lebowitz, J. Chem. Phys. **34**, 1037 (1961).
[44] M. A. Cotter and F. H. Stillinger, J. Chem. Phys. **57**, 3356 (1972).
[45] B. Widom, J. Phys. Chem. **99**, 2803 (1995).
[46] A. I. Rusanov, Colloids Surf., A **159**, 315 (1999).
[47] B. Derjaguin, Kolloid-Z. **69**, 155 (1934).